Journal of Molecular Structure 1354 (2026) 144847

Contents lists available at ScienceDirect

Journal of Molecular Structure

journal homepage: www.elsevier.com/locate/molstr

Application of degree-based topological descriptors, molecular properties, chemical reactivity prediction and nonlinear optical analysis of 5-[2-[4-(1,2-benzothiazol-3-yl) piperazin-1-yl] ethyl]-6-chloro-1,3-dihydroindol-2-one

S. Kayashrini [a], P. Rajesh [a,*], M. Kesavan [b], A. Kala [c], M. Pavithra [d]

[a] Department of Physics, School of Basic Sciences, Vels Institute of Science, Technology & Advanced Studies (VISTAS), Pallavaram, Chennai 600117, Tamil Nadu, India
[b] Interdisciplinary Institute of Indian System of Medicine, SRM Institute of Science and Technology, Kattankulathur, Chennai, 603203, Tamil Nadu, India
[c] Department of Physics, Government Arts College (Autonomous), Nandanam, Chennai 600 035, Tamil Nadu, India
[d] Department of Condensed Matter Physics, Saveetha School of Engineering, Saveetha Institute of Medical and Technical Sciences (SIMATS), Chennai, 602105, Tamil Nadu, India

ARTICLE INFO

Keywords:
ZPSD
NBO
Topological studies
Anticancer
QSPR analysis

ABSTRACT

This study demonstrates the potential role of Ziprasidone (ZPSD) as a liver anticancer drug by combining computational and experimental methods to examine the pharmacological, structural, and electrical properties of the molecule. The molecule appears to have favourable stability and chemical reactivity, as indicated by the HOMO-LUMO energy gap of 4.3995 eV found in Density Functional Theory (DFT) calculations using the B3LYP/6–311++*G*(d,p) basis set. Important electrophilic (such as C_2, S_{20}, and N_1) and nucleophilic (such as O_{10}, N_{14}, and N_{21}) centres necessary for biomolecular interactions were identified by Natural Bond Orbital (NBO) interactions more especially, the N_1—H_{29} (σ) → C_2—C_3 (σ*) and σ → σ* transitions and Mulliken population analyses, which also revealed strong electron delocalization. For comprehensive molecular visualization and analysis, the study used Veda 04 software for PED values in addition to Gaussian 09 W, Gauss View 6.0, and ChemCraft 1.8. UV–Vis spectra and TD-DFT predictions further supported the presence of functionally relevant groups such as carbonyl, NH, CH, and aromatic systems, which were confirmed by vibrational (FT-IR) and NMR spectroscopy. Understanding electronic density distributions, which are correlated with the molecule's dipole moment and possible interaction zones was made possible by the Molecular Electrostatic Potential (MEP), Electron Localization Function (ELF), and Localized Orbital Locator (LOL) maps. The potential anticancer activity of ZPSD is enhanced by its moderate dipole moment (8.91×10^{-30} Cm^{-1}) and high hyperpolarizability (βtot) $9.3 \times 10^{-40} C^3 \cdot m^3 \cdot J^{-2}$. In accordance with Docking studies revealed that the proteins (PDB IDs: 3T6G and 6NM0) had favourable binding energies (-7.72 and -6.75 kcal/mol), stable hydrogen bonds at significant residues (SER582, TYR114, LYS149) and the BOILED-Egg model, QSPR descriptors by topological indices, drug-likeness by Lipinski's rule confirmed ZPSD as a liver anti-cancer activity.

1. Introduction

Ziprasidone was first created as a second-generation a typical antipsychotic to treat bipolar disorder and schizophrenia. However, its growing potential as an anti-cancer drug, particularly in the treatment of breast cancer, has recently drawn interest from cancer researchers [1]. ZPSD is a 1,2-benzothiazol-3-yl- and 2-(6-chloro-1,3-dihydro-2-oxindol-5-yl) ethyl substituents joined to the nitrogen atoms and piperazine compound also. It functions as an antipsychotic, histamine, muscarinic, serotonergic, dopaminergic, and psychotropic drug. Though originally developed for psychiatric use, emerging studies suggest that ZPSD may exert anti-proliferative, pro-apoptotic, and cell cycle–regulatory effects on breast cancer cells [2]. Preclinical studies have shown that ZPSD may inhibit the growth of breast cancer cell lines, possibly through mechanisms involving oxidative stress induction, mitochondrial dysfunction, or modulation of signalling pathways such

* Corresponding author.
E-mail address: rajesh.ncc5coy@gmail.com (P. Rajesh).

https://doi.org/10.1016/j.molstruc.2025.144847
Received 13 August 2025; Received in revised form 8 November 2025; Accepted 22 November 2025
Available online 23 November 2025

as PI3K/AKT or MAPK/ERK. These pathways are often dysregulated in breast cancer and are key targets for therapeutic intervention. While research is still at an early stage and primarily limited to in vitro or animal models, the repurposing of ZPSD and other antipsychotics offers a novel and cost-effective approach to cancer drug discovery [3–5]. Its potential to enhance the effectiveness of existing therapies or reduce tumour progression highlights the need for further investigation, especially through clinical trials [6,7]. It is a good candidate for therapeutic repurposing due to its distinct electronic structure and bioactive scaffold. Because ZPSD has conjugated π-systems and heteroatoms that can form strong hydrogen bonds and polarization, it shares important characteristics with anticancer pharmacophores [8]. Although other antipsychotics have demonstrated cytotoxic and apoptotic effects in cancer cells [9], there are still few studies that connect ZPSD's quantum characteristics to its anticancer potential, which supports the choice of ZPSD for this study [10]. To the best of my knowledge, no one is able to complete this work through DFT. The goal of this study is to investigate the anticancer activity, specifically for liver cancer, that can be attained through the compound using the DFT studies by exposing it to UV–Vis analysis, FT-IR analysis, and NMR studies in order to validate the compound and predict the efficacy of the application findings [11].The research ELF, LOL, Electron-Hole Analysis and RDG analyses offer a more thorough explanation of the physical and chemical features with optimized structure using the B3LYP/6–311++*G*(d,p) basis and DFT calculations, while NBO and HOMO-LUMO provide geometrical qualities. Nonlinear Optical (NLO) and molecular docking experiments will be carried out in addition to DFT-based structural and electronic investigations to assess the optical response and biological interaction potential of the ZPSD molecule. The molecule's aptitude for optoelectronic applications is revealed by the NLO analysis, and its potential bioactive behaviour and binding affinity toward biological targets are revealed by molecular docking from natural sources in order to create analyte-specific receptors and ascertain the compound ZPSD capacity through docking studies using Autodock 4.0. A cleaner and healthier environment will be created by correcting the anticancer activity of liver cancer in addition to the mathematical studies that are included to clarify the ZPSD.

2. Methodology of ZPSD

The study uses a methodical and sequential approach that integrates biological, theoretical, and experimental analyses. The molecular structure and functional groups were confirmed by FT-IR, UV–Vis and NMR spectroscopy. MEP, ELF, and LOL representations of charge distribution was used to support the optimized geometry, electronic parameters, and reactive centres that were obtained from DFT and NBO calculations. While QSPR and the BOILED-Egg model assessed pharmacokinetic and drug-likeness properties, the optimized structure led molecular docking to analyse protein–ligand interactions and anticancer potential.

2.1. Experimental details

The pharmaceutical component ZPSD was utilized without any additional purification after being purchased in powdered form from reputable chemical source Sigma-Aldrich. Its optical and structural characteristics were described using a variety of sophisticated spectroscopic methods [12]. A Perkin Elmer Lambda 35 UV Win Lab V6.0 spectrometer operating at room temperature was used to perform UV–Visible absorption spectroscopy, which covered a wide wavelength range of 185–3300 nm with a variable bandwidth of 0.5–4.0 nm. Among the light sources were a tungsten-halogen lamp for the visible spectrum and a deuterium lamp for the ultraviolet [13]. A PERKIN ELMER FT-IR spectrometer with a resolution of 4 cm^{-1}, a high scanning speed of 20 spectra per second, and a signal-to-noise ratio of 60,000:1 was used to perform FT-IR spectroscopy utilizing the KBr pellet method for vibrational analysis. The spectral data were gathered between 7800 and 350 cm^{-1} in order to determine the compound's functional groups. The chemical structure was further clarified by using Nuclear Magnetic Resonance (NMR) spectroscopy. A Bruker high-resolution instrument at 300 K and a Varian Mercury Plus 500 MHz spectrometer were used to record the ^{1}H and ^{13}C spectra [14]. At SRM College of Science in Kattankulathur, Tamil Nadu, India, the measurements were carried out using a base frequency of 400 MHz for ^{1}H nuclei and 100 MHz for ^{13}C nuclei. The molecular features of ZPSD were thoroughly analysed and confirmed thanks to this multi-technique approach.

2.2. Computational details

Gaussian 09 W software was used for all theoretical analyses in this investigation. GaussView 6.0 and ChemCraft 1.8 were used to visualize the molecular geometry, specifically bond lengths and bond angles, as well as HOMO-LUMO orbitals and molecular electrostatic potential (MEP) surfaces [15]. To identify reactive sites within the Ziprasidone (ZPSD) molecule, important parameters were used, including the MEP surface, Mulliken charge distribution, NMR shifts, energy gap features, electrophilicity, and nucleophilicity indices. Using the hybrid B3LYP functional and the 6–311++*G*(d,p) basis set, Density Functional Theory (DFT) calculations were performed [16]. Using VEDA 04, vibrational frequencies associated with FT-IR spectra and PED percentages were calculated; the results demonstrated a high degree of agreement with experimental data. UV–Visible spectra and density of states (DOS) in gas phase and DMSO solvent were simulated using the TD-DFT method. Moreover, the interpretation of stabilization energies, antibonding interactions, and natural bond orbital (NBO) properties such as hyperconjugation, donor–acceptor interactions, and intramolecular hydrogen bonding was made possible by second-order perturbation theory in Gaussian 09 W. Using MULTIWFN 3.7 (Win 64), topological descriptors like LOL, RDG, Electron-Hole analysis, and ELF were assessed. Lastly, AutoDock 4.0 molecular docking studies were used to evaluate ligand–receptor binding interactions, offering information on the binding efficiency of ZPSD with target proteins [17].

3. Result and discussion

3.1. Optimized structure

The ideal molecular geometry is displayed in Fig. 1. along with the chemical structure and ZPSD numbering. The initial geometry of ZPSD was constructed using GaussView 6.0 and pre-optimized with the MMFF94 force field to remove steric strain. This low-energy conformation was then used as the input structure for full geometry optimization at the DFT/B3LYP/6–311++*G*(d,p) level in Gaussian 09, which is used to determine geometrical features such as bond length and bond angle [18]. It belongs to the 1,2-benzisothiazole, indolone, piperazine and organochlorine compound families, where, Formula for the chemical: $C_{21}H_{21}ClN_4OS$ Weight in molecules: 412.9 g/mol, Solid appearance, the melting point is around 276 °C.The Bond Angle and Bond Length are part of the structure's optimal molecular geometry, as shown in the Table 1. ZPSD is a heterocyclic compound with a complex polycyclic structure that includes heteroatoms and several functional groups [19]. Its fundamental structure consists of an aryl linkage connecting a dihydroindolone segment, a piperazine moiety, and a benzisothiazole ring. In addition, the molecule has nitrogen, sulfur, and a chlorine substituent, all of which support its electronic and pharmacological characteristics. Delocalized π-bonding is indicated by the fused, aromatic benzisothiazole ring, which has C–C bond lengths that are usually between 1.38 and 1.40 Å. The *C═O* group carbonyl in this moiety exhibits a characteristic short bond length 1.21 Å by B3LYP, and the dihydroindolone unit is connected by a flexible ethyl chain. With N–C bond lengths that vary depending on their surroundings, the piperazine ring takes on a chair-like shape and joins the aromatic system via

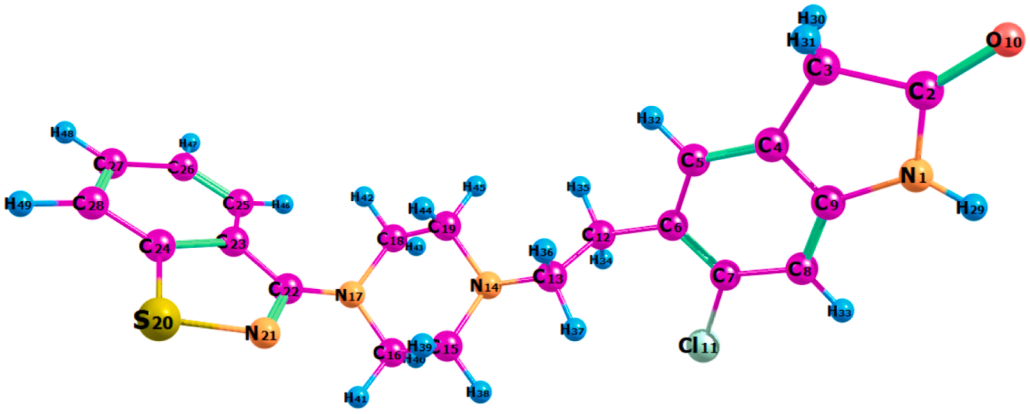

Fig. 1. ZPSD optimized structure.

Table 1
Structural Parameter of the ZPSD.

Bond length Å	B3LYP	XRD data	Bond length Å, Angle (°)	B3LYP	XRD data	Bond Angle (°)	B3LYP	XRD data
N_1—C_2	1.39	1.28	$C_{27}C_{28}$	1.38	1.38	$N_{14}C_{15}H_{38}$	108.46	111.6
N_1—C_9	1.39	1.39	$C_{27}H_{48}$	1.08	1.00	$N_{14}C_{15}H_{39}$	112.20	111.7
N_1—H_{29}	1.00	0.86	$C_{28}H_{49}$	1.08	0.97	$C_{16}C_{15}H_{38}$	109.00	109.00
C_2—C_3	1.54	1.40	$C_2N_1C_9$	112.54	114.51	$C_{16}C_{15}H_{39}$	109.25	109.00
C_2—O_{10}	1.21	1.28	$C_2N_1H_{29}$	121.74	-	$H_{38}C_{15}H_{39}$	107.80	109.00
C_3-C_4	1.50	1.47	$C_9N_1H_{29}$	125.71	-	$C_{15}C_{16}N_{17}$	112.91	111.30
C_3-H_{30}	1.09	0.96	$N_1C_2C_3$	106.16	108.00	$C_{15}C_{16}H_{40}$	108.72	109.00
C_3-H_{31}	1.09	0.93	$N_1C_2O_{10}$	125.60	-	$C_{15}C_{16}H_{41}$	110.33	110.00
C_4-C_5	1.38	1.35	$C_3C_2O_{10}$	128.23	125.69	$N_{17}C_{16}H_{40}$	107.08	108.00
C_4-C_9	1.40	1.38	$C_2C_3C_4$	103.66	-	$N_{17}C_{16}H_{41}$	108.63	109.00
C_5-C_6	1.41	1.36	$C_2C_3H_{30}$	109.16	109.00	$H_{40}C_{16}H_{41}$	109.04	109.00
C_5-H_{32}	1.08	0.96	$C_2C_3H_{31}$	109.16	109.00	$C_{16}N_{17}C_{18}$	110.97	109.50
C_6-C_7	1.40	1.43	$C_2C_3H_{30}$	113.86	112.00	$C_{16}N_{17}H_{22}$	117.73	-
C_9-C_{12}	1.51	1.51	$C_2C_3H_{30}$	113.85	112.00	$C_{18}N_{17}C_{22}$	118.74	119.00
C_7-C_8	1.40	1.39	$H_{30}C_3H_{31}$	106.99	108.00	$N_{17}C_{18}C_{19}$	112.06	111.30
C_7-Cl_{11}	1.76	-	$C_3C_4C_5$	132.28	-	$N_{17}C_{18}H_{42}$	109.90	109.00
C_8-C_9	1.38	1.37	$C_3C_4C_9$	108.32	-	$N_{17}C_{18}H_{43}$	108.13	108.00
C^8-H^{33}	1.08	1.00	$C_5C_4C_9$	119.39	-	$C_{19}C_{18}H_{42}$	109.32	109.00
Cl^{11}-H^{37}	3.05	-	$C_4C_5C_6$	121.36	-	$C_{19}C_{18}H_{43}$	108.97	109.00
C^{12}-C^{13}	1.54	1.50	$C_4C_5H_{32}$	120.14	120.00	$H_{42}C_{18}H_{43}$	108.35	109.00
C^{12}-H^{34}	1.09	0.97	$C_6C_5H_{32}$	118.48	117.00	$N_{14}C_{19}C_{18}$	110.68	110.00
C^{12}-H^{35}	1.09	1.00	$C_5C_6C_7$	116.96	-	$N_{14}C_{19}H_{44}$	111.59	110.00
C^{13}-N^{14}	1.46	1.40	$C_5C_6H_{12}$	119.81	119.00	$N_{14}C_{19}H_{45}$	109.51	109.00
C^{13}-H^{36}	1.10	1.00	$C_7C_6H_{12}$	123.20	123.00	$C_{18}C_{19}H_{44}$	109.22	110.00
C^{13}-H^{37}	1.09	0.93	$C_6C_7C_8$	123.32	-	$C_{18}C_{19}H_{45}$	108.38	110.00
N^{14}-C^{15}	1.46	1.46	$C_6C_7Cl_{11}$	120.12	-	$H_{44}C_{19}H_{45}$	107.32	107.00
N^{14}-C^{19}	1.46	1.47	$C_8C_7Cl_{11}$	116.54	-	$C_{21}S_{20}C_{24}$	94.00	91.75
C^{15}-C^{16}	1.53	1.49	$C_7C_8C_9$	117.28	-	$S_{20}N_{21}C_{22}$	122.08	122.10
C^{15}-H^{38}	1.09	1.00	$C_7C_8H_{33}$	120.40	-	$N_{17}C_{22}N_{21}$	120.79	-
C^{15}-H^{39}	1.10	0.96	$C_9C_8H_{33}$	122.3	123.00	$N_{17}C_{22}C_{23}$	123.1	124.15
C^{16}- N^{17}	1.46	1.47	$N_1C_9C_4$	109.30	109.50	$N_{21}C_{22}C_{23}$	115.97	116.62
C^{16}-H^{40}	1.09	1.00	$N_1C_9C_8$	129.03	127.50	$C_{22}C_{23}C_{24}$	109.90	-
C^{16}-H^{41}	1.09	0.97	$C_4C_9C_8$	121.65	-	$C_{22}C_{23}C_{25}$	130.91	-
N^{17} -C^{18}	1.47	1.47	$C_7Cl_{11}H_{37}$	75.42	-	$C_{24}C_{23}C_{25}$	119.05	-
N^{17}-C^{22}	1.39	1.37	$C_6C_{12}H_{13}$	112.56	109.00	$S_{20}C_{24}C_{23}$	108.9	110.65
C^{18}-C^{19}	1.53	1.50	$C_6C_{12}H_{34}$	110.85	109.00	$S_{20}C_{24}C_{28}$	129.36	-
C^{18}-H^{42}	1.09	0.96	$C_6C_{12}H_{35}$	108.26	109.00	$C_{23}C_{24}C_{28}$	121.57	122.18
C^{18}-H^{43}	1.09	1.00	$C_{13}C_{12}H_{34}$	108.09	109.00	$C_{23}C_{25}C_{26}$	119.43	119.62
C^{19}-H^{44}	1.10	0.93	$C_{13}C_{12}H_{35}$	109.92	109.00	$C_{23}C_{25}H_{46}$	120.40	120.00
C^{19}-H^{45}	1.09	0.97	$H_{34}C_{12}H_{35}$	106.98	108.00	$C_{26}C_{25}H_{46}$	120.10	-
S^{20}-N^{21}	1.70	-	$C_{12}C_{13}C_{14}$	112.60	-	$C_{25}C_{26}C_{27}$	120.69	-
S^{20}-C^{24}	1.74	1.73	$C_{12}C_{13}H_{36}$	109.50	109.00	$C_{25}C_{26}H_{47}$	119.72	120.00
N^{21}-C^{22}	1.31	1.28	$C_{12}C_{13}H_{37}$	108.19	109.00	$C_{27}C_{26}H_{47}$	119.57	120.00
C^{22}-C^{23}	1.46	1.49	$C_{14}C_{13}H_{36}$	112.03	-	$C_{26}C_{27}C_{28}$	120.89	121.23
C^{23}-C^{24}	1.41	1.43	$C_{14}C_{13}H_{37}$	107.69	109.00	$C_{26}C_{27}H_{48}$	119.57	117.00
C^{23}-C^{25}	1.40	-	$H_{36}C_{13}H_{37}$	106.5	108.00	$C_{28}C_{27}H_{48}$	119.5	117.00
C^{24}-C^{28}	1.40	1.39	$C_{13}C_{14}C_{15}$	112.08	-	$C_{24}C_{28}C_{27}$	118.26	119.58
C^{25}-C^{26}	1.38	1.35	$C_{13}C_{14}C_{19}$	112.94	-	$C_{24}C_{28}H_{49}$	120.91	120.00
C^{25}-H^{46}	1.08	1.01	$C_{15}C_{14}C_{19}$	109.91	-	$C_{27}C_{28}H_{49}$	120.81	-
C^{26}-C^{27}	1.40	-	$N_{14}C_{15}C_{16}$	110.0	109.50	$Cl_{11}H_{37}C_{13}$	114.33	-

nitrogen atoms [20–24]. At about 1.70 Å, the S–N bond from the thiazole portion is comparatively long, indicating a single bond with partial delocalization. The presence of a chloro substituent is confirmed by the C–Cl bond, which is visible at about 1.76 Å. Although these are shorter in XRD because of experimental constraints, hydrogen atoms exhibit B3LYP-optimized bond lengths of 1.08–1.10 Standard hybridization geometries are reflected in the bond angles: sp^3 centres show angles close to 109.5°, whereas sp^2 centres, particularly in aromatic rings and amide linkages, show angles between 118° and 130° [25,26]. The molecule exhibits both planar and non-planar regions, suggesting a balance between flexibility in the piperazine ring and aliphatic chains and rigidity in the aromatic and amide regions, the majority of nitrogen–carbon (N–C) and carbon–carbon (C–C) bond lengths predicted by B3LYP fall within the expected range of 1.38 to 1.54 Å. Due to conjugation or crystal packing effects, the N_1– C_2 bond exhibits a notable deviation, measuring 1.39 Å in B3LYP and 1.28 Å in XRD. Theoretical and experimental agreement for aromatic C—C bonds, like C_{27}–C_{28}, is very good. C—H bond lengths, on the other hand, vary more significantly; B3LYP predicts lengths of 1.08–1.10 Å, while XRD data displays shorter values (0.86–1.01 Å), which is to be expected given the limitations of X-ray diffraction in precisely locating hydrogen atoms. Particularly for typical tetrahedral centres, where angles cluster around 109.5°, the bond angles determined using B3LYP are also generally in agreement with the XRD data. However, there are discernible variations in some angles involving nitrogen or in strained ring systems. The C_2–N_1–C_9 angle, for instance, is measured at 114.51° (XRD) and computed at 112.54° (B3LYP). Theoretically, the N_1–C_2–O_{10} angle is 125.60° The C_7–Cl_{11}–H_{37} geometry exhibits angle as 75.42° in B3LYP, which suggests strain or a unique conformation. The C_7–Cl_{11}–H_{37} geometry exhibits a strain or a unique conformation. Typical aromatic or flexible structural motifs are matched by chain and ring angles that fall between 118° and 130°, such as C_{25}–C_{26}–C_{27} and C_{24}–C_{28}–C_{27} [27–29]. The Table 1 explain the theoretical values were well matched to the experimental values of it.

3.2. Mulliken charges

Mulliken population analysis uses a molecule electron distribution to estimate atomic charges. These charges impact characteristics like electronic structure, polarizability, and dipole moment and reveal the bonding nature. Mulliken population analysis from the gaussian optimization was provided through the valuable insight into the electronic distribution of a molecule by estimating atomic charges through $q_A = Z_A - \sum_{\mu \in A} \sum_{\nu} P_{\mu\nu} S_{\mu\nu}$, where Z_A = atomic number, $P_{\mu\nu}$ = density matrix, and $S_{\mu\nu}$ = overlap matrix, the total electron density among the atoms in a molecule to describe charge transfer and bonding character can be investigated on ZPSD molecule through the B3LYP and the 6–311++*G* (d, p) basis sets, using Gaussian 09 which is listed in Table 2 [30,31].In Fig. 2. Shows the electrophilic character is demonstrated by the oxygen atom charge of O_{10} ‣ −0.44571 eV, N_{14} ‣ −0.44225 eV, N_{17} ‣ −0.48465 eV, N_{21}‣ −0.61349 eV and the positive charges on some carbon atoms, S_{20} ‣ 0.323474 eV, Cl_{11} ‣0.07539 eV, N_1‣ 0.657889 eV, C_2 ‣ 0.551495 eV, C_4 ‣ 0.055148 eV, C_6 ‣ 0.129973 eV, C_9 ‣ 0.346082 eV, C_{22} ‣ 0.463936 eV, C_{23} ‣ 0.108303 eV. The charges of hydrogen atoms vary from H_{29} ‣ 0.28368 eV to H_{31}‣ 0.157114 eV. With the maximum charge at H_{29} ‣ 0.28368 eV, the hydrogen atoms show comparatively homogeneous charges, indicating a variety of bonding conditions. This technique finds the molecule's electron-rich (nucleophilic) and electron-deficient (electrophilic) areas. Strong nucleophilic character is suggested by highly negative charges on atoms like O_{10}, N_{14}, N_{17}, and N_{21} in the ZPSD molecule, whereas electrophilic behaviour is indicated by positive charges on atoms like C_2, N_1, and S_{20}.The findings show that the oxygen atoms have areas of high electron density, which makes them possible nucleophilic sites, and the highly charged carbon atoms are likely electrophilic sites, which are necessary for binding contacts and reactivity [27–29].

3.3. NBO analysis

In molecular systems, the NBO analysis is a useful method for elucidating intramolecular and intermolecular bonding as well as interactions between bonds. The analysis of charge transfers or hyperconjugation interactions inside the molecules is also made easier. The high E (2) value in this framework indicates a high level of interaction between electron donors and acceptors as well as a higher degree of systemic conjugation [32]. The stabilization energies of the title molecule have been examined using the donor-acceptor interactions in the NBO basis were assessed using the second-order Fock-matrix. The localized NBO of the idealized Lewis structure loses occupancy as a result of the interactions, becoming an empty non-Lewis orbital. The stabilization energy E (2) connected to the delocalization i/j for every donor (i) and acceptor (j) is calculated as

$$E^{(2)} = \Delta E_{ij} = q_i \frac{F(i,j)^2}{\varepsilon_j - \varepsilon_i}$$

where the energy of the NBO donor and acceptor is represented by E_i and E_j, respectively, the orbital stabilization energy by E (2), the occupancy of the donating orbitals by q_i, and the Fock matrix element connecting NBO orbitals i and j by $F_{i,j}$ [33]. Table 3 shows the NBO calculations for a few chosen donors and acceptors. The Instinct Connection The way the molecule's electrons interact and support its structure is demonstrated via orbital analysis. Among the molecule's double bonds are some of the strongest interactions. The stabilization energies of 21.7 kcal/mol and 21.0 kcal/mol are obtained from interactions between the electrons from the π bond between C_4 and C_5 and the π* antibonds of C_6–C_7 and C_8–C_9. The region between π(C_6–C_7) and π*(C_8–C_9) exhibits substantial electron sharing or delocalization, as evidenced by an extremely high stabilization energy of 284 kcal/mol. Cl_{11} and S_{20} atoms' lone pair electrons are also crucial. More stability is added by the interactions between the lone pair from Cl_{11} and π*(C_6–C_7) (13.0 kcal/mol) and π* (C_{23}–C_{24}) (23.4 kcal/mol). In addition, σ bonds that donate electrons to neighboring σ* antibonds, as (C_3–C_4) to σ*(C_2–O_{10} and σ(N_1–C_9) to σ* (C_2–O_{10}), with energies of about 3.7 kcal/mol and 3.4 kcal/mol, are useful interactions. The characteristics of bonding and charge

Table 2
Mulliken Atomic Charges of ZPSD.

Atom	Energy	Atom	Energy	Atom	Energy	Atom	Energy	Atom	Energy
N_1	0.6578	Cl_{11}	0.0753	N_{21}	−0.6134	H_{31}	0.1571	H_{41}	0.1491
C_2	0.5514	C_{12}	−0.2567	C_2	0.4639	H_{32}	0.0923	H_{42}	0.1190
C_3	−0.2982	C_{13}	−0.0579	C_{23}	0.1083	H_{33}	0.1062	H_{43}	0.1054
C_4	0.0551	N_{14}	−0.4422	C_{24}	−0.1604	H_{34}	0.1230	H_{44}	0.0772
C_5	−0.1631	C_{15}	−0.0295	C_{25}	−0.1137	H_{35}	0.1051	H_{45}	0.1043
C_6	0.1299	C_{16}	−0.0698	C_{26}	−0.1162	H_{36}	0.0701	H_{46}	0.1055
C_7	−0.1451	N_{17}	−0.4846	C_{27}	−0.0704	H_{37}	0.1067	H_{47}	0.0876
C_8	−0.1279	C_{18}	−0.0768	C_{28}	−0.1164	H_{38}	0.0998	H_{48}	0.0903
C_9	0.3460	C_{19}	−0.0326	H_{29}	0.2836	H_{39}	0.0862	H_{49}	0.0993
O_{10}	−0.4457	S_{20}	0.3234	H_{30}	0.1489	H_{40}	0.1077		

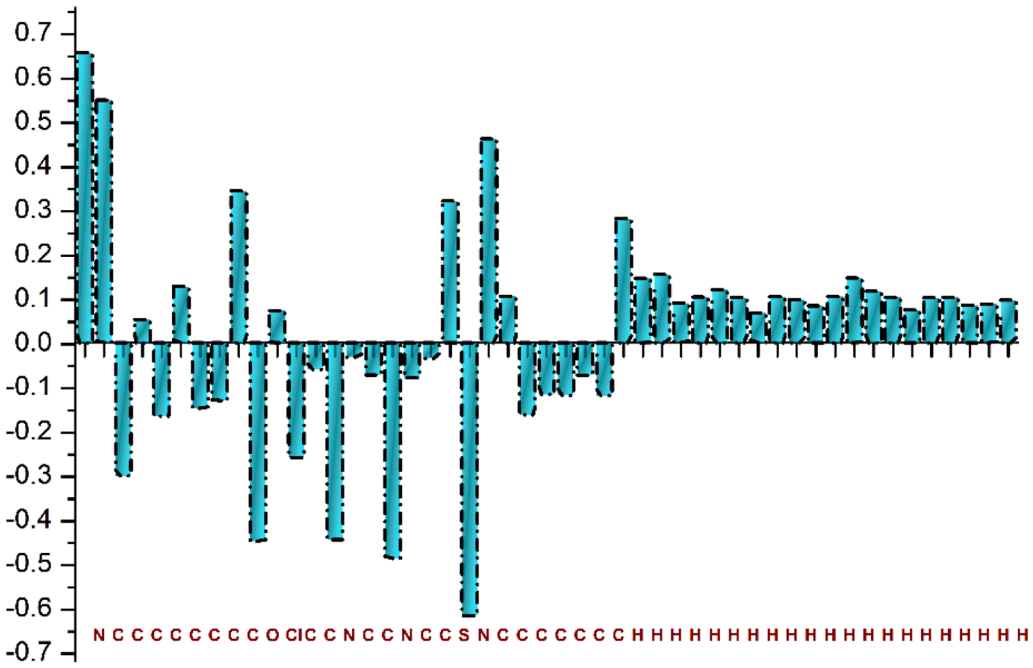

Fig. 2. Mulliken atomic charges of ZPSD.

Table 3
Donor and Acceptor interaction NBOs analysis on ZPSD molecules.

Donor NBO (i)	Acceptor NBO (j)	E (2) kcal/mol	E(j)-E(i) a.u.	F(i,j) a.u.	Donor NBO (i)	Acceptor NBO (j)	E (2) kcal/mol	E(j)-E(i) a.u.	F(i,j) a.u.
LP (2) Cl_{11}	π^*C_6–C_7	13.0	0.35	0.06	π^*N_1–C_2	σ^*C_2–O_{10}	0.69	0.29	0.05
σC_7–Cl_{11}	σ^*C_{13}–H_{37}	0.72	1.24	0.02	π^*C_2–O_{10}	σ^*C_3–H_{31}	1.01	0.40	0.05
σN_{14}–C_{15}	σ^*C_{13}–N_{14}	0.83	1.08	0.02	π^*C_2–O_{10}	π^*C_4–C_5	0.5	0.03	0.00
σN_{14}–C_{19}	σ^*C_{18}–H_{42}	1.02	1.10	0.03	σ C_8–C_9	σ^*N_1–C_9	1.38	1.13	0.03
σC_{16}–N_{17}	σ^*N_{17}–C_{18}	0.76	1.03	0.02	σC_{16}–H_{41}	σ^*N_{14}–C_{15}	4.09	0.85	0.05
σN_{17}–C_{18}	σ^*C_{16}–H_{41}	1.23	1.15	0.03	σS_{20}–C_{24}	σ^*S_{20}–N_{21}	2.05	0.89	0.03
σS_{20}–C_{24}	σ^*N_{17}–C_{22}	0.98	1.33	0.03	σN_1–C_2	σ^*C_8- C_9	4.87	1.33	0.07
πN_{21}–C_{22}	σ^*N_{17}–C_{18}	0.57	0.63	0.01	σN_1–H_{29}	σ^*C_2–C_3	1.22	1.03	0.03
σC_{22}–C_{23}	σ^*N_{17}–C_{22}	3.54	1.35	0.06	σC_4–C_9	σ^*N_1–H_{29}	2.77	1.09	0.04
σN_1–C_9	σ^*C_2–O_{10}	3.48	1.39	0.06	σC_7–Cl_{11}	σ^*C_8–C_9	2.01	1.35	0.04
σN_{17}–C_{22}	σ^*S_{20}–N_{21}	1.83	1.14	0.04	LP(3)Cl_{11}	σ^*C_6–C_7	1.28	1.00	0.03
σS_{20}–N_{21}	σ^*N_{17}–C_{22}	8.76	1.35	0.09	LP (2)S_{20}	π^*C_{23}–C_{24}	23.4	0.25	0.07

delocalization in ZPSD are revealed by the hybrid composition of main donor and acceptor orbitals. The strong p-character of the σ(N1–C2) bond is indicated by the hybrid orbitals on N1 and C2, which are sp^1, sp^2 (33.7 % s, 66.3 % p) and 32.8 % s, 67.2 % p, respectively. O10 and N17′s lone pair orbitals are primarily p-type (>85 %), which promotes π-delocalization with nearby π* orbitals. The reported E (2) value of 23.4 kcal mol^{-1} for the LP (2)S20 → π*C23–C24 transition is consistent with the LP (2)S20 orbital's ~35 % s and ~65 % p contribution, indicating its possible involvement in conjugative interactions. According to these interactions, electrons are not stationary; rather, they migrate throughout the molecule to maintain its stability and reactivity. Understanding this behaviour is crucial to comprehending the characteristics of the molecule and its potential interactions in biological systems.

3.4. UV–Vis, HOMO LUMO, MEP, DOS analysis of ZPSD

The electronic transition features of ZPSD were found through the UV–Visible spectra and related properties of oscillation strengths (f), excitation energy (eV), and absorption band (nm) shown in Figs. 3 and Fig. 4. Quantum chemical theory was used to interpret these features based on the DFT/B3LYP/6–311++*G*(d,p) method, which was calculated in the gas phase and correlated with experimental UV–Visible spectra. We have analysed the UV spectra with DOS states using time-dependent density functional theory (TD-DFT) on the optimized structure in gas. The Shimadzu UV–Vis spectrometer was used to measure the UV–Vis. A simple and direct method for figuring out the band gap energy of organic p conjugated systems is UV–Vis [34,35]. The following equation can be used to determine the optical band gap: Eg = 1242/ λth, where λth is the threshold wavelength (in nm), determined from the beginning of the absorption spectrum, and Eg is the optical energy band gap (in eV). When using the Gaussian 09 W program to model the electron density and charge distribution of the three-dimensional intermolecular interaction of reactive behaviour, the Molecular Electrostatic Potential is helpful. Since we are aware that the potential between adjacent atoms determines their interactions, V(r) shows the potential that exists in the space around a molecule because of its nuclei and electrons. It is a good way to tell how the molecule will react. In math, it looks like this:

$$V(r) = \sum \frac{Z_R}{R_A - r} - \int \frac{\rho(r')}{(r' - r)} \mathrm{d}r$$

where Z_A is the charge of nucleus A located at position R_A and ρ(r′) represents the electronic density function of the molecule, with r′ as the integration variable. At any point r = (x,y,z) near the molecule, the MEP, V(r), corresponds to the interaction energy between the molecule charge distribution (electrons and nuclei) and a positive test charge (proton)

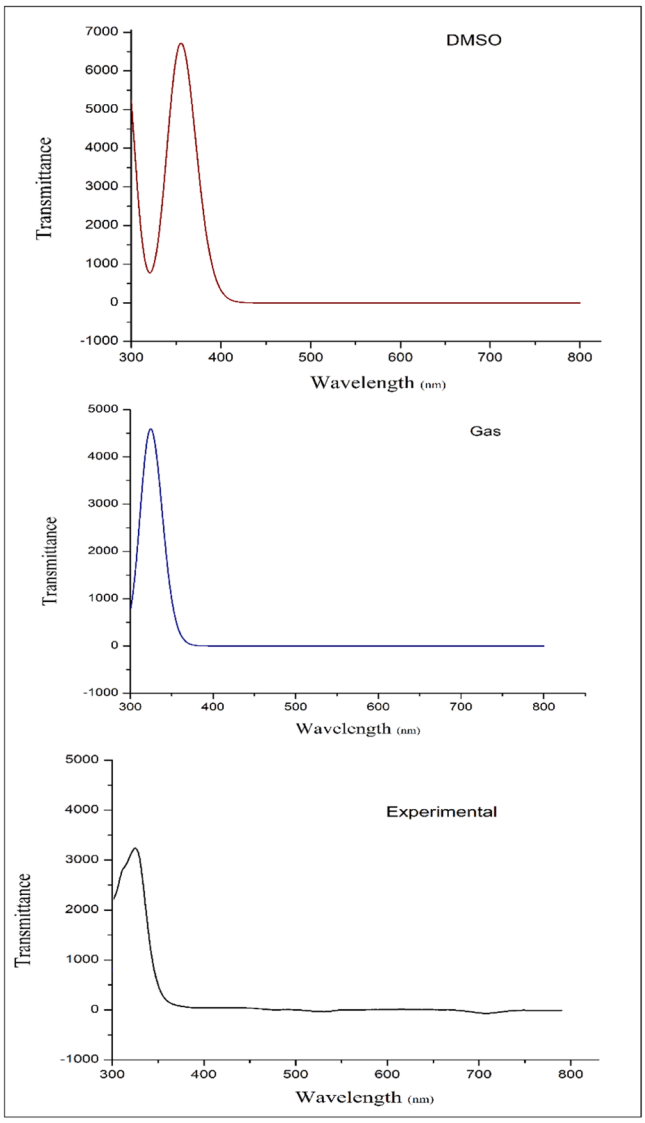

Fig. 3. UV–Vis, TD-DFT of ZPSD.

placed at r [36]. The optimized shape of the title molecule is used to create the MEP map, which is seen in Fig. 5. shows crisp views of border molecular orbitals using Gauss View 5.0 software.

All of these characteristics experience significant HOMO-LUMO orbital changes upon absorption of UV radiation. The n-p transition is less noticeable than the p-p transition. The n or p orbitals shift to an excited state in the absorption spectroscopy approach. Additionally, after reporting the molecular orbitals' energy, we computed the energy gap between the major peaks of the spectra's molecular orbitals and the border HOMO–LUMO orbitals. The UV spectrum in gas phase and the DMSO is depicted in Fig. 3. and the molecule's computed wavelength, energy, bond gap, and oscillator strength are shown in the Table 4. The Homo-Lumo energy gap is shown in the Fig. 4. to have a sizable energy gap of 4.3995 eV, with Homo-Lumo values of −5.4194 eV and −1.0198 eV. using Koopman's theorem the compound's stability is validated by its chemical hardness, which in this investigation is −3.4640 eV. An electrophilicity index maximum range of 2.3560 eV, which indicates biological activity, is confirmed by the observation [37]. The ZPSD chemical is non-toxic, as indicated by its low softness value of 0.4545 eV^{-1}.

Its electronic stability is further reinforced by its ionization potential of 5.4194 eV and electron affinity of 1.0198 eV. Moderate reactivity is suggested by electronegativity 3.2196 eV and electrophilicity 3.6588 eV, with a greater electron-donating capacity ω− = 1.0212 eV than electron-accepting capacity ω+ = 1.0212 eV. The computed chemical reactivity descriptors are listed in Table 5. These properties indicate that ZPSD is a molecule with biological action [38]. The UV–Vis spectrum of ZPSD shows bands corresponding to intramolecular electronic transitions, primarily π→π* within the aromatic rings and n→π* involving the carbonyl and nitrogen lone pairs. HOMO orbitals are mainly localized on the electron-rich aromatic and benzisothiazole regions, while LUMO orbitals are concentrated on the electron-deficient carbonyl and dihydroindolone moieties, indicating intramolecular charge transfer. The HOMO–LUMO gap reflects moderate electronic excitation energy, supporting the observed UV transitions and highlighting key regions of electron density redistribution in the molecule. The UV–Vis at the gas phase with the 3 states denote the energy gap values which is similar to the both theoretical and experimental energy gap values as for wavelength respect to the 283.27 nm / 4.3995 eV, 306.67 nm /4.0429 eV. The calculated UV–Vis absorption at 324.37 nm was scaled using a factor of 0.999 to match the experimental value of 324 nm. Applying this factor to other calculated peaks gives scaled values of 282.99, 281.76, 354.69, 306.36, and 291.76 nm, improving agreement with experimental observations.

According to the MEP surface contour map, which Key characteristics of the electrostatic landscape of ZPSD are revealed by the electron rich red region to blue region. which ranges from -5.698×10^{-2} to $+5.698 \times 10^{-2}$ atomic units. Potential sites for electrophilic attack and hydrogen bond acceptance are indicated by the concentrated electron-rich regions (red) surrounding the carbonyl oxygen atom (O_{10}) and nitrogen atoms, which is ability to interact with biomolecular targets like DNA, kinases, or apoptotic regulators is suggested by heteroatoms [39]. Particularly close to hydrogen atoms on nitrogen atoms (N_1, N_{14}, N_{17}, N_{21}) with electronegativity associated with the electron rich red region, electron-deficient regions (blue) indicate probable hydrogen bond donors and nucleophilic interaction sites. Meanwhile, the chlorine atom (Cl_{11}) is moderately positive, contributing a range from neutral to slightly positive potential. The aromatic and hydrophobic portions of the molecule are separated by neutral to moderately polar (green to yellow) positive regions of sulfur atom (S_{20}), which aid in receptor binding via van der Waals and hydrophobic interactions. where the electron density is lower in the title molecule, as shown in Mulliken table [37,38]. Similar to other heterocyclic compounds with similar pharmacophores, these interactions may cause apoptosis or interfere with the signalling pathways of cancer cells.

3.5. *FT-IR and vibrational assignment*

The DFT-B3LYP functional with the 6–311++*G*(d,p) basis set was used to conduct the vibrational analysis of ZPSD. With 49 atoms, the optimized molecule, which roughly corresponds to the C_2 point group, produces 141 normal vibrational modes (3N–6). To verify the optimized structure, the computed frequencies were scaled and compared to the experimental FT-IR spectra Figs. 6a. and Fig. 6b The most important vibrations were observed from the Table 6 as CH, CC, OC, CCO, HCCC, HCC, HCH, and HCCO, HCO, HCOC, CCCC, CCC, OCO, OCOC, OCCC, which summarizes the corresponding theoretical and experimental wavenumbers as well as potential energy distribution (PED) data also [39,40].

ZPSD's FT-IR spectrum shows distinctive absorption bands that are dispersed throughout three main regions and each of which corresponds to a distinct molecular vibration. Strong N–H and C–H stretching vibrations are seen in the high-frequency range (3000–3700 cm^{-1}). The presence of amine or amide functionalities is confirmed by the experimental band close to 3414 cm^{-1} and the theoretical υNH mode at 3657 cm^{-1}. The coexistence of aromatic and aliphatic hydrogen environments is indicated by the aromatic and aliphatic C–H stretching vibrations (υCH), which appear between 3221 and 2931 cm^{-1} in close agreement with theoretical predictions. Different *C═O* and *C═C/C═N* stretching

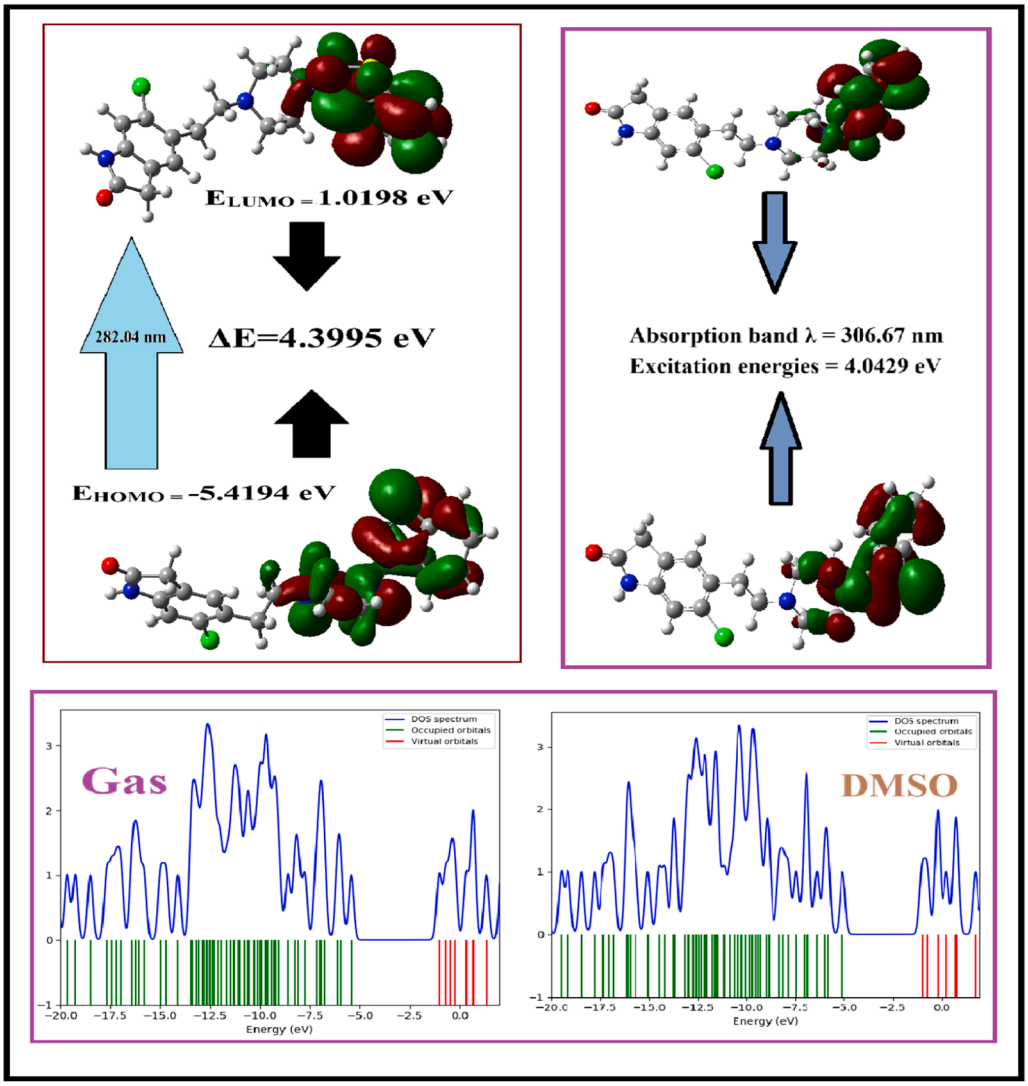

Fig. 4. E_{HOMO}-E_{LUMO} of ZPSD with solvents.

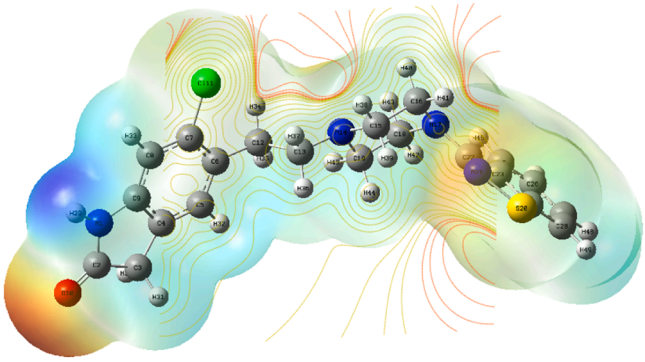

Fig. 5. MEP map surface on ZPSD.

modes are visible in the mid-frequency region (1500–1800 cm^{-1}) at 1849 cm^{-1} and 1679–1551 cm^{-1}, respectively. The presence of a carbonyl group is confirmed by the strong *C═O* absorption, and the conjugated heteroaromatic framework of ZPSD is confirmed by the *C═C* and *C═N* bands. Skeletal deformations within the aromatic core are reflected in complex in-plane bending (δ) and torsional (τ) vibrations like δHCH, δHCC, τHCCC, and τHNCC in the fingerprint region (1500–500 cm^{-1}). The presence of halogen and sulphur substitutions in the molecule is confirmed by additional bands at about 698 cm^{-1} and 413 cm^{-1}, which correspond to C–Cl and S–C stretching vibrations, respectively. The B3LYP/6–311++*G*(d,p) calculated vibrational frequencies were scaled using a factor of 0.967 to improve agreement with experimental FT-IR as the 3657 cm^{-1} NH stretch scales to 3537 cm^{-1}, 3198 cm^{-1} CH stretches scale to 3091 cm^{-1}, 1634 cm^{-1} CC stretch scales to 1580 cm^{-1}, and 1499 cm^{-1} HCH+CC mode scales to 1449 cm^{-1}, showing better correlation with experimental values.

The optimized geometry and proper orientation of the functional groups in ZPSD are confirmed by the high correlation between experimental and theoretical frequencies. PED analysis validates the vibrational assignments by showing significant contributions from CH, CC, OC, and HCCO coordinates. The structure of the molecule includes conjugated aromatic and heteroaromatic moieties (piperazine and indole) with Cl, O, and N substitutions that improve molecular stability, polarity, and π–π stacking. In line with its possible anticancer activity, the presence of hydrogen-bond donor (NH) and acceptor (O, Cl) sites facilitates biomolecular recognition. Overall, there is a strong experimental-theoretical correlation in the vibrational profile, which validates the compound's structural soundness and range of functions [39,40].

Table 4
TDDFT for the ZPSD.

Solvents	States	B3LYP/6–311G(d,p)				Major & Minor Contributions Energy (%)
		Absorption band λ (nm)	Band gap (eV)	Oscillation Strength	Energy (cm^{-1})	
Gas Phase	**S1**	324.37 nm	3.8223 eV	0.0634	30,828	HOMO->LUMO (96 %)
	S2	283.27 nm	4.3769 eV	0.0011	35,302	HOMO->L + 1 (96 %), H-1->L + 1 (2 %)
	S3	282.04 nm	4.3960 eV	0.0054	35,456	H-1->LUMO (84 %), H-2->LUMO (12 %), HOMO->L + 3 (2 %)
DMSO	**S1**	355.04 nm	3.4921 eV	0.0927	28,165	HOMO->LUMO (96 %), HOMO->L + 2 (2 %)
	S2	306.67 nm	4.0429 eV	0.0000	32,608	HOMO->L + 1 (100 %)
	S3	292.05 nm	4.2454 eV	0.0906	34,241	HOMO->L + 2 (91 %), H-6->LUMO (2 %)

Experimental => 324 nm.

Table 5
Chemical stability & reactivity on ZPSD.

Electronic Properties	Values eV	Electronic Properties	Values eV
E_{HOMO}	−5.4194 eV	Chemical hardness (η)	−3.4640 eV
E_{LUMO}	−1.0198 eV	Chemical softness (σ)	0.4545 eV^{-1}
ΔE	4.3995 eV	Electrophilicity Index (ω)	2.3560eV
Ionization potential (IP)	5.4194 eV	Nucleophilicity Index	0.1366 eV^{-1}
Electron affinity (EA)	1.0198 eV	Electron donor power (ω^-)	4.0212 eV
Electronegativity(χ)	3.2196 eV	Electron acceptor power (ω^+)	1.0212 eV
Chemical potential (μ)	−3.2196 eV	ΔNmax (eV)	−1.7221 eV

3.6. Topological analysis

3.6.1. ELF and LOL analysis

Electron localization in atomic and molecular systems is evaluated using the electron localization function. ELF and LOL aid in determining the location with the highest electron density. The gradient increases when the localized orbitals overlap. These topological properties were visualized using the Multiwfn program, and the color maps confirmed the presence of bonding and non-bonding electrons. The ELF map spans from 0.0 to 1.0 and is color-coded blue to red, whereas the LOL map ranges from 0.0 to 0.8.

According to the interpretation of the ELF and LOL maps Fig. 7., location with red and yellow colouring near 1.0 suggest a high amount of electron localization. These zones are commonly found around lone pairs, bonded pairs, or π-electrons particularly near atoms like nitrogen (N), oxygen (O), and halogens like chlorine (CL), and fluorine (F). These locations indicate strong covalent bonding or the localization of lone pairs. The blue and dark blue regions (with lower values, near to 0) represent electron-deficient areas, which corresponds to non-bonding spaces such as interatomic gaps, where electrons are seldom localized and are commonly found between the inner and valence shell of atoms. The white region in the LOL map indicates a high amount of electron localization. This might be due to strong bonding contacts, a lone pair, an electron-rich location or an orbital overlap. This region indicates that electron density surpasses the colour scale's maximum threshold of 0.8 [41,42].

3.6.2. Reduced density gradient of ZPSD

To investigate the various types of non-covalent interactions between molecules and as a crucial instrument for comprehending research on chemical reactivity. RDG analysis is a visual method that makes covalent interactions more complex. Figs. 8a and Fig. 8b show the color-filled RDG map and scatter map of the compound RDG, which were produced using the software analyser VMD 1.9.2 and Multiwfn 3.7. The nature and distribution of weak intermolecular forces that affect the studied molecule's biological activity and binding potential are revealed by the analysis of its Reduced Density Gradient (RDG) and Non-Covalent Interaction (NCI) [43,44]. Different interaction types are indicated by distinct regions in the RDG vs. sign(λ_2) ρ plot. Strong attractive interactions like hydrogen bonding and electrostatic attractions are indicated by the blue region, which corresponds to sign(λ_2) ρ values that range from roughly –0.035 to –0.020 a.u. These are essential for keeping protein-ligand complexes stable while docking. The weak van der Waals forces shown by the green region, which is centred close to 0.00 a.u., improve surface complementarity and molecular stability in a binding pocket even though they are small on their own. Although steric repulsion is indicated by the red region, which has sign(λ_2)ρ values greater than 0.015 a.u., the comparatively sparse appearance of these regions implies that the molecule has a favourable steric profile with

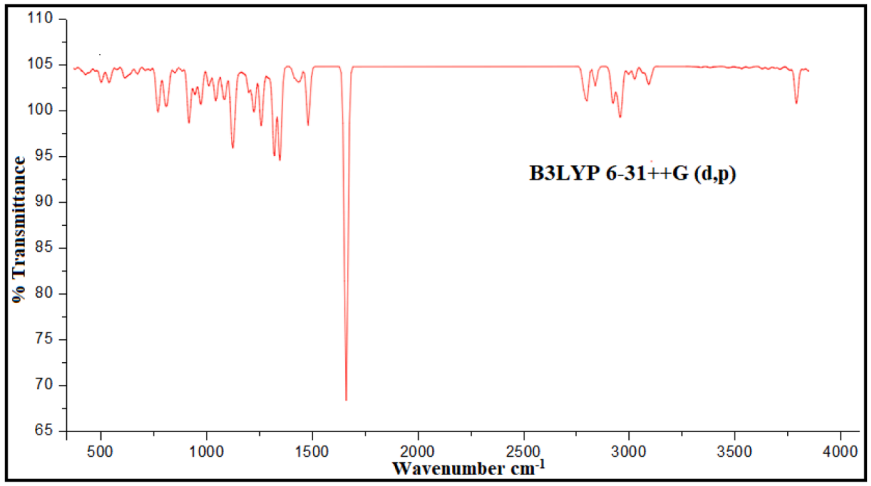

Fig. 6a. Theoretical Vibrational Assignment of ZPSD.

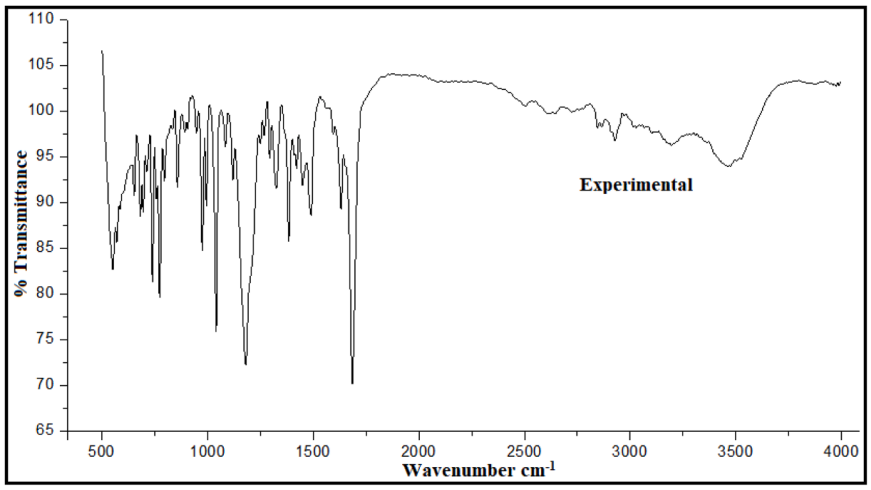

Fig. 6b. Experimental FT-IR of ZPSD.

little internal strain.

This analysis is further supported by the 3D NCI isosurface visualization, which shows hydrogen bonding potential between polar functional groups and significant van der Waals interactions indicated by green patches scattered throughout the molecular structure. The molecule's capacity to firmly fit into target protein active sites is improved by these carefully placed interactions. Stable binding orientations are supported by the low number of red isosurfaces, which confirms that steric clashes are minimal. The compound's ability to form potent and targeted non-covalent interactions, which are essential for high-affinity docking is confirmed by the combined RDG and NCI results. Given its balanced profile of attractive and dispersive forces and low steric hindrance, these results strongly imply that the molecule is well-suited for interaction with biological receptors and could be a promising lead compound in drug discovery [45,46].

3.7. NMR analysis

Nuclear magnetic resonance (NMR) is a strong analytical technology used in physics, chemistry, biology, and medicine to examine molecular dynamics and structure. The GIAO technique's projected chemical shifts for the ZPSD of 13C and 1H NMR are displayed in the Table 8. Because NMR reveals the groupings of hydrogen and carbon, it is useful for detecting organic compounds [47]. To make the predictions, the B3LYP/6–311++*G* (d,p) approach was used through the Table 7 and Fig. 9. The NMR data provided-both theoretical and experimental chemical shifts for carbon (^{13}C) and hydrogen (^{1}H) demonstrate strong structural agreement and confirm the integrity of the predicted molecule, which is a complex heterocyclic compound likely designed for biological or anticancer activity. Shifts between 27.49 and 55.72 ppm are observed in the aliphatic carbon atoms (C_2, C_3, C_{12}–C_{22}), which is consistent with sp^3 carbons joined to nitrogen atoms or in saturated ring systems such as piperazine or other N-containing heterocycles. Proper substitution and ring strain predictions are confirmed by the small differences between theoretical and experimental values, which are usually <1 ppm. Likewise, protons H30–H49 exhibit slight deshielding from electron-withdrawing effects (Cl, amide, etc.) and resonate in the 2.07–4.75 ppm range, which is typical for protons next to nitrogen or halogen atoms. Interestingly, C22 (55.72 ppm) and H45 (4.14 ppm) correspond to a methylene group that is probably next to an amide nitrogen or heteroatom, resulting in a downfield shift and deshielding. Shifts between 124.62 and 153.62 ppm are seen in the aromatic carbons (C_4–C_{28}), which are in good agreement with conjugated aromatic systems and heterocycles such as pyridine, thiazole, or benzene. Within the heteroaromatic ring system, C_{24} (145.84 ppm) and C_{27} (153.62 ppm) are most likely *C*═*N* or *C*═*C* carbons [48].

A highly deshielded environment, possibly a carbonyl or conjugated imine, is seen in C_6 (163.64 ppm), which is suggestive of a reactive pharmacophore like an amide or thiazolidinone. A hydrogen-bond donor (NH) group, which is essential for intermolecular interactions with biological targets, is represented by the downfield proton H_{37} (10.53 ppm). Reliable structure modeling is demonstrated by experimental values that closely match theoretical prediction.

This region's protons, H_{29} to H_{46} (7.05 to 9.29 ppm), are in the usual aromatic range; downfield shifts suggest conjugated π-systems or substituents that withdraw electrons. Particularly deshielded are H_{42} (9.97 ppm) and H_{46} (8.18 ppm), for instance, indicating closeness to electronegative atoms or involvement in π-π stacking or hydrogen bonding. The molecule's structural integrity is confirmed by the close correspondence between the experimental and theoretical ^{13}C and ^{1}H NMR chemical shifts. Deshielding patterns, particularly in the aromatic and heteroaromatic regions, support the presence of electron-withdrawing groups (Cl, *C*═*O*, N, S) and a conjugated, planar system that can form hydrogen bonds and stack π–π, which are crucial properties for binding to biomolecular targets in cancer treatment. The compound's potential as a lead compound for the development of anticancer drugs is supported by its NMR profile, which shows a well-distributed electronic environment, functional diversity, and structural stability [49].

3.8. Electron-Hole analysis

The nature of the electronic excitations and the behaviour of charge transfer are better understood by examining the electron–hole analysis for the three excited states in the gas phase listed in Table 8. State I have the lowest excitation energy (5.612 eV), and the electron and hole stay close to one another in a localized excitation, as indicated by the H index (1.942 Å) and D index (0.223 Å). The tiny separation points to an intrafragment π–π transition with a low level of charge transfer. Although the electron and hole are on opposite sides of the molecular center, the overall strength of the interaction is maintained because of their close proximity, as indicated by the negative t index (−1.107 Å). In State II, the H index dramatically increases to 3.824 Å and the excitation energy rises to 6.691 eV, indicating a moderate charge transfer character. The excitation involves movement of electronic density over a longer range, possibly between different parts of the molecule (donor to acceptor), as indicated by the D index (1.156 Å), which shows a noticeable increase in electron–hole separation. Although the electron and hole are still on opposite sides, the increased distance indicates a partial delocalization or semi-local charge transfer, as indicated by the increasingly negative t index (−1.375 Å). With the highest excitation energy (6.951 eV), State

Table 6
Vibrational Assignment of ZPSD.

Mode No.	B3LYP (cm^{-1})	Experimental (cm^{-1})	Vibrational Assignment	PED (%)	IR Intensity (km/mol)	Raman Activity ($Å^4$/amu)
1	3657	3414	υNH	100	58.1642	177.9202
2	3221	-	υCH	100	1.9432	97.0627
3	3218	-	υCH	83	10.852	197.039
4	3207	-	υCH	95	24.3676	167.801
5	3198	3196	υCH	90	7.1208	116.2181
6	3186	3190	υCH	92	0.8723	64.7856
7	3180	-	υCH	100	10.1337	65.8097
8	3146	-	υCH	91	7.8321	59.3789
9	3144	-	υCH	90	15.4396	67.4606
10	3118	-	υCH	89	13.4905	28.869
11	3103	-	υCH	100	2.3397	89.1282
12	3087	-	υCH	83	29.417	38.9795
13	3082	-	υCH	87	46.463	176.4545
14	3073	3070	υCH	86	38.0617	89.7016
15	3066	-	υCH	100	7.1534	174.3236
16	3061	-	υCH	80	15.4379	63.3826
17	3049	-	υCH	79	48.2488	114.8081
18	3042	-	υCH	79	19.9116	43.3101
19	2969		υCH	93	36.1359	58.2515
20	2931	2932	υCH	92	58.1294	48.9315
21	2916		υCH	93	33.5091	24.1365
22	1849		υOC	87	622.1589	27.633
23	1679		υCC	63	109.3243	124.2484
24	1646		υCC	47	16.3865	15.8939
25	1634	1631	υCC	62	22.3144	14.8611
26	1617	1627	υCC	62	18.9512	28.1792
27	1551	1560	υCC	31	173.3826	59.5073
28	1551	1560	υNC	10	157.4216	14.3232
29	1526	-	δHCC	12	7.6756	15.9071
30	1524	-	δHCH	70	3.8625	12.1148
31	1510	-	δHCH	78	5.1862	16.5267
32	1505	-	δHCH	73	5.3095	21.5347
33	1499	1493	δHCH	84	8.4739	5.6644
34	1499	1493	υCC	14	2.2994	13.3027
35	1498	-	δHCH	75	13.0889	13.0566
36	1491	1493	δHCH	26	9.9541	11.1236
37	1469	1473	δHCH	12	96.3499	27.8168
38	1469	1473	υCC	14	3.9215	28.4474
39	1439	-	δHCC+ υCC	27+12	36.6712	22.0089
40	1467	1460	υCC	10	54.6618	89.6579
41	1480	-	δHCH	69	28.5239	52.454
42	1449	-	δHCH	74	6.1662	11.5175
43	1432	-	υCC	17	11.7591	43.7931
44	1410	-	υCC	10	12.2409	4.8237
45	1413	-	υCC	40	2.6951	30.3044
46	1411	-	δHCN	32	7.9306	2.089
47	1410	-	δHNC	33	45.606	10.338
48	1389	-	δHCC	41	45.4988	39.3319
49	1372	-	υCC+ δHCC	77+10	95.6415	20.6112
50	1370	1290	δHCC	50	7.6457	3.1984
51	1349	-	δHCC	38	4.2792	12.9434
52	1342	-	δHNC	26	44.8726	2.0094
53	1336	1246	δHNC	27	13.0086	15.0449
54	1322	-	δHNC	27	18.3532	9.9003
55	1312	-	δHNC	29	27.4338	1.2621
56	1304	1203	δHNC	28	40.8994	36.3361
57	1312	-	δHCC	10	7.8743	4.4962
58	1297	-	δHCC	32	22.1322	12.5292
59	1290	-	δHCC+ δHCH	10+34	13.619	4.6409
60	1269	-	δHNC	48	39.3723	6.243
61	1262	-	υCC	39	27.1785	6.7077
62	1249	-	δHCC	33	13.5368	5.0778
63	1234	-	δHNC	49	4.4757	2.9553
64	1230	-	δHNC	44	45.6931	14.1696
65	1200	1083	υCC	30	6.1869	12.3771
66	1194	-	δHCC	43	0.3834	6.3593
67	1188	-	υCC	14	6.1863	6.5001
68	1181	-	υCC	19	100.0683	1.59
69	1170	-	υNC	27	8.2767	5.92
70	1160	-	δHCC	84	7.8971	0.18
71	1151	-	υCC	10	4.1558	18.15
72	1151	-	υClC	21	11.9078	4.16
73	1143	1000	υCC	44	6.2512	23.91

(*continued on next page*)

Table 6 (*continued*)

Mode No.	B3LYP (cm^{-1})	Experimental (cm^{-1})	Vibrational Assignment	PED (%)	IR Intensity (km/mol)	Raman Activity (Å⁴/amu)
74	1113	-	υCC	24	43.3488	15.71
75	1082	972	δHCN	50	43.1414	6.80
76	1076		δHCC	41	32.5897	3.66
77	1052	947	δHCC	12	61.2957	1.35
78	1052	947	υCC	48	0.0803	0.18
79	1051	-	υCC	18	6.3631	0.65
80	1044	-	υCC	29	0.9409	0.56
81	1033	-	δHCN	42	6.2749	2.60
82	1009	-	υCC	27	13.6297	1.18
83	1002	-	υCC	43	1.4496	1.45
84	990	-	τHCCH	94	10.6463	0.72
85	969	835	δHCC	15	0.3805	3.08
86	954	-	τHCCC	86	11.6367	14.23
87	946	-	υCC	44	17.5136	2.11
88	912	-	υCC	31	0.4887	3.32
89	969	-	δHCC	13	5.5064	14.53
90	969	-	τHNCC	21	11.2502	1.94
91	882	-	υCC	32	4.3823	2.03
92	867	-	υCC	62	19.3231	2.65
93	853	-	τHCCC	83	2.0775	4.54
94	852	-	τHCNC	38	6.515	8.52
95	820	-	υCC	0	25.8093	2.92
96	791	-	υNC	2	0.6371	4.47
97	787	-	δHCC	34	7.676	15.04
98	781	-	τHCCC	73	9.2075	2.81
99	763	773	υCC	29	3.5593	5.64
100	758	-	δHCC	38	12.2776	2.73
101	747	743	τHCCC	60	6.1636	0.56
102	728	736	τHNCC	51	4.8683	3.99
103	722	-	υSC	11	11.3238	5.18
104	722	-	δHCC	25	48.4598	0.93
105	698	-	υClC	14	21.8308	3.89
106	686	-	δHNC	53	7.2097	4.70
107	659	-	τHNCC	50	6.1341	4.60
108	630	-	δHCC	42	2.3514	3.05
109	592	-	δHCC	48	3.7159	1.46
110	571	-	τHNCC	12	2.681	1.59
111	565	-	δHNC	32	66.8174	3.08
112	532	-	δHNC	16	1.0028	3.06
113	513	-	δCNC+ τHCCC	22+34	4.7097	0.36
114	507	-	δCNC+ τHCCC	12+17	3.2477	1.79
115	489	-	δHCC	43	0.1815	1.00
116	438	-	δCCO	15	1.0958	3.98
117	444	-	δHCC	10	3.9865	3.23
118	413	-	υSC	14	2.9499	1.56
119	404	-	τHNCO	25	1.729	2.12

δ -bending, υ- stretching, β -scissoring, t-twisting, ρ- rocking, ω- wagging,.

III has unique properties. A highly delocalized charge transfer excitation is indicated by the exceptionally high D index (7.249 Å) and the highest Δr index (4.579) among the three states, while the H index (2.599 Å) is marginally lower than in State II. It's interesting to note that the t index changes to a large, positive value (+4.994 Å), indicating that the electron and hole are on the same side of the molecule but are separated by a large amount of space. This arrangement is typical of long-range intramolecular charge transfer, which is frequently observed in optoelectronic systems where efficient electron–hole separation is crucial. In general, the evolution from State I to State III demonstrates a shift from a localized excitation to progressively more robust charge transfer behaviour, with important ramifications for the photophysical and electronic properties of the molecule is shown in the Figs. 10a. and Fig. 10b [50,51].

3.9. NLO properties

DFT-based hyperpolarizability and polarizability calculations were used to examine the synthetic molecule's nonlinear optical characteristics. From the Table 9, average polarizability (α) that was calculated was: αtot = -1.8740×10^{-23} esu. The anisotropy of polarizability (Δα), which represents the directional dependency of the polarizability tensor, was as follows: α tot = -1.8740×10^{-23}esu. Δα = 6.3411×10^{-23}esu. Δα=6.3411×10^{-23} esu. The first hyperpolarizability ($\beta_{t_o t}$) of the molecule was: βtot = 302.47 a.u.= 2.6131×10^{-30} esu, β tot = 302.47 a.u. = 2.6131×10^{-30} esu, which is substantially greater than 7 % that of urea, the conventional reference molecule (β ≈ 0.3728×10^{-30} esu) [52]. This suggests that second-order nonlinear optical applications, like electro-optic modulation and second harmonic generation (SHG), have a lot of promise. Calculating the total dipole moment was done as follows: μtot = 2.67 Debye Moderate molecular polarity is suggested by Debye.

The **βxxx** is dominant and negative, indicating a strong NLO response along the x-axis. **βxzz** and **βzxx** are positive and relatively large, suggesting significant delocalization and conjugation along mixed axes. Other components like **βzzz** and **βxyz** are smaller but contribute to the overall NLO behaviour. The individual tensor components such as βxxx = −342.18, βxzz = 47.32, and βzxx = 64.07 further indicate a strong directional charge flow along the molecular axis, enhancing π–π stacking and hydrogen bonding potential, which are essential for anticancer activity through DNA intercalation or kinase inhibition. The anisotropy of polarizability (Δα) is notably high (427.87 a.u., 6.3411 × 10^{-23} esu), confirming an uneven electronic cloud distribution that

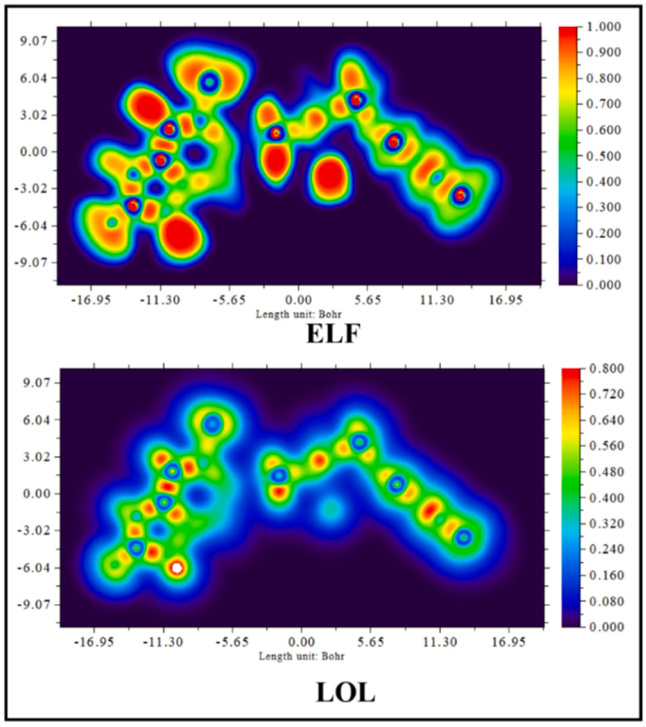

Fig. 7. ELF and LOL analysis of ZPSD.

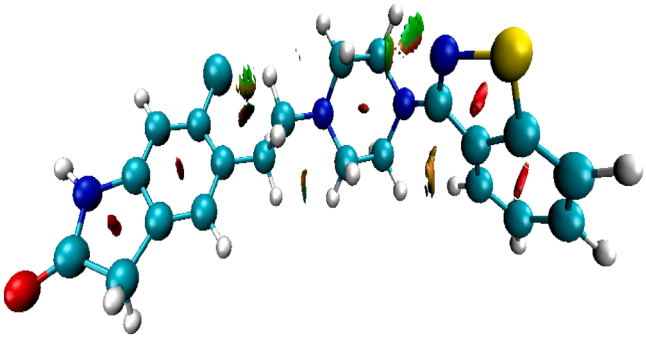

Fig. 8a. Van der Waals, Steric effect with Hydrogen bonding of ZPSD.

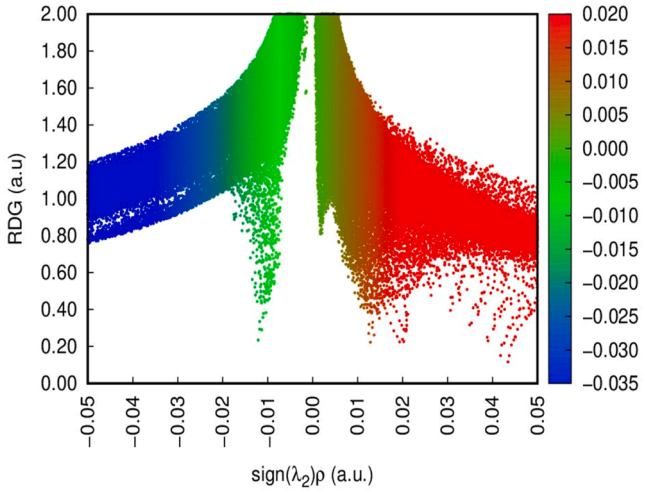

Fig. 8b. Sign (λ_2) ρ plot of ZPSD.

Table 7
NMR Analysis of ZPSD.

Atom	Theoretical Chemical Shift in ppm	Experimental chemical shift in ppm	Atom	Theoretical Chemical Shift in ppm	Experimental chemical shift in ppm
C18	27.49	27.65	H48	2.07	2.39
C19	36.42	35.93	H39	2.65	2.50
C3	38.42	39.49	H34	2.75	2.51
C12	38.70	39.99	H44	3.88	3.14
C16	39.76	40.16	H47	3.60	3.15
C15	39.93	40.50	H49	3.23	3.38
C13	46.87	47.28	H30	3.53	3.50
C2	50.31	51.45	H38	3.68	3.73
C22	55.25	55.72	H45	4.75	4.14
C7	111.70	110.50	H43	7.05	6.89
C8	124.62	125.30	H31	7.13	7.30
C9	126.39	126.17	H41	7.30	7.46
C23	127.69	126.74	H36	7.46	7.49
C5	128.83	127.74	H33	7.72	7.59
C4	128.66	127.44	H40	8.05	7.60
C25	129.56	128.03	H29	8.13	7.62
C28	130.63	129.67	H32	8.62	8.12
C26	132.68	132.16	H35	8.68	8.16
C24	145.84	145.58	H46	8.98	8.18
C27	153.01	153.62	H42	9.29	9.97
C6	163.27	163.64	H37	10.40	10.53

facilitates selective binding with asymmetric biological targets like enzyme active sites or receptor pockets and the SI unit values for the βtot $= 9.3 \times 10^{-40}$ $C^3m^3J^{-2}$; $\Delta\alpha = 7.06 \times ^{10-63}$ Cm^2V^{-1}; μ (D) $= 8.91 \times 10-30$ Cm^{-1} [53,54].

3.10. Druglikness

This prediction informs users about the medicine's effectiveness and whether or not the ligand under investigation possesses characteristics that are typical of an oral active agent.

This prediction is based Lipinski's rule of five with ZPSD total polar surface area, number of hydrogen donors, hydrogen acceptors, and rotatable bonds are all provided by the SwissADME predictor shown in the Table 10. Based on the SwissADME computed data, all of the synthesized compounds in this study have zero breaches of Lipinski's rule of five. Chemicals may therefore be appropriate for studies on their antibacterial, antioxidant, and anticancer qualities. It may become more drug-like and effective if its structure is altered by adding polar groups or shortening the chain [55]. The image depicts a BOILED-Egg model, commonly used in computational drug discovery to evaluate the absorption and brain penetration potential of small molecules. The y-axis plot denotes lipophilicity (WLOGP), and the x-axis shows the Topological Polar Surface Area (TPSA) shown in Fig. 11.

The yellow region represents the area where molecules are predicted to have high gastrointestinal absorption (HIA), while the white region suggests potential blood-brain barrier (BBB) penetration. The blue dot within the yellow region but outside the white region indicates that the compound is likely to be well absorbed in the gastrointestinal tract but unlikely to penetrate the blood-brain barrier. This suggests the molecule is a good candidate for oral administration but may not be effective for central nervous system targets. The image illustrates the pH-dependent microspecies distribution and molecular structures of certain derivatives with potential anticancer properties. The predominant form at physiological pH (~7.4) is represented by the red curve in the microspecies distribution graph, indicating that this protonation state is the most significant for biological activity. The three molecules have a common scaffold that is probably based on indole or a related heterocyclic system, which is known to have anticancer properties like inducing apoptosis, inhibiting enzymes, or intercalating DNA. Chlorine atoms may improve cellular permeability and lipophilicity, whereas rings containing nitrogen may make it easier to bind with biological targets via ionic or hydrogen bonding processes. The red icons beneath each

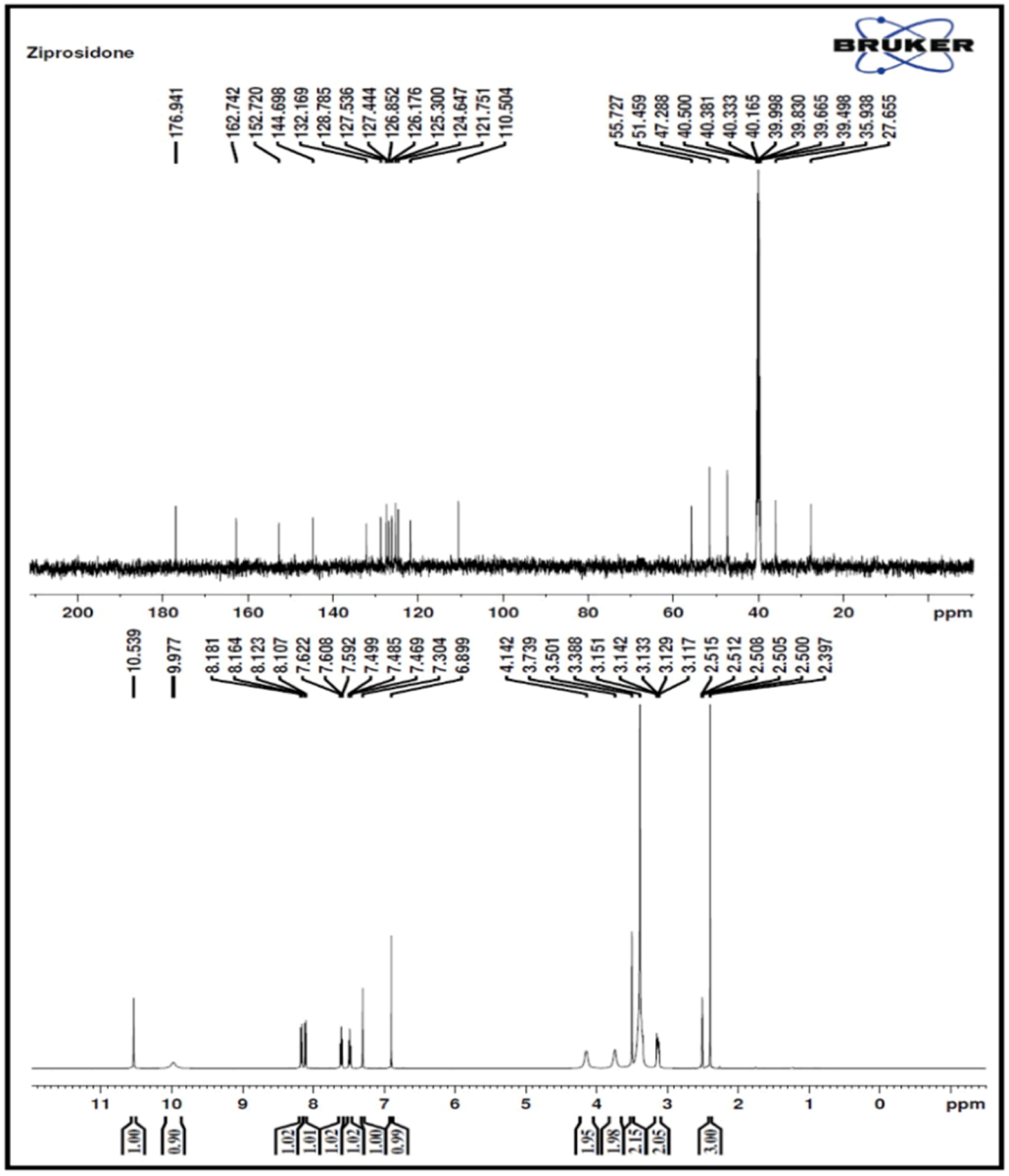

Fig. 9. NMR of H^1 and C^{13} of ZPSD.

Table 8
Electron-Hole Analysis of ZPSD.

Solvent	State	Excitation energy E (eV)	H index (Å)	D index (Å)	Δr index	t index (Å)
Gas	**I**	5.612	1.942	0.223	4.347	1.107
	II	6.691	3.824	1.156	3.415	1.375
	III	6.951	2.599	7.249	4.579	4.994

structure indicate favourable drug-like properties, such as hydrogen bond donors/acceptors and moderate lipophilicity, supporting good bioavailability and cell membrane penetration. Furthermore, the compounds may continue to function in both neutral and acidic environments, including the acidic microenvironment of tumours, given their capacity to exist in various ionization states based on pH. All things considered, the physicochemical and structural properties of these derivatives are in good agreement with those of typical anticancer agents [56].

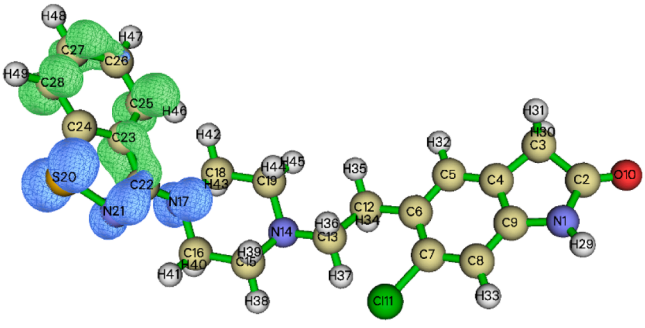

Fig. 10a. Electron-Hole of ZPSD.

3.11. *Docking and ramachandra plot*

Molecular docking was performed in this investigation using the Autodock 4.0 program, which predicts interactions between small compounds and a target protein's binding site and offers insights into

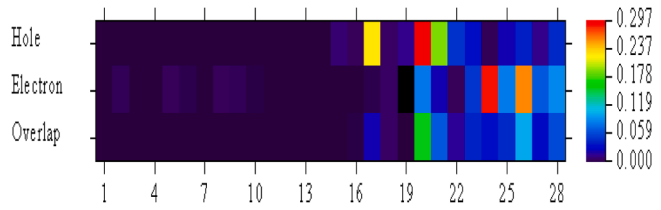

Fig. 10b. Hole-electron overlap matrix heatmap of ZPSD.

basic biological phenomena. Molecular docking studies against two pertinent protein targets, 3T6G and 6NM0, have demonstrated through Figs. 12a and 12b along with Table 11, the majority of residues 95 % occupy preferred α-helix and β-sheet regions, as indicated by the Ramachandran plot of 6NM0, guaranteeing a stable backbone and precise binding site geometry. A tiny fraction 8 % is in allowed loop or turn regions, which offer flexibility that can help with ligand accommodation.

Similar to this, 3T6G exhibits a dependable structure with flexible loops for ligand binding, with the majority of its residues 92 % in favoured regions, 7 % in allowed flexible regions. Both proteins are appropriate for molecular docking with ziprasidone because they have flexible binding site regions and structurally sound backbones overall. These proteins are frequently linked to pathways related to cancer, including enzymatic targets involved in tumour progression, signal transduction, and cell cycle regulation [57]. At a bond distance of 2.0 Å, ZPSD established a single hydrogen bond with SER582 (O···NH) for the 3T6G complex. This bond had an estimated inhibition constant of 16.91 μM and a binding energy of –6.75 kcal mol^{-1} exhibited a corresponding intermolecular energy (−7.7 kcal/mol) and ligand efficiency (−0.23), hydrogen-bonding and van der Waals forces (−7.27 kcal/mol) with an electrostatic contribution (−0.44 kcal/mol). The ligand was stabilized inside the binding pocket by hydrophobic interactions with the residues of THR199, LEU198, PRO202, THR200, ALA65, ASN67, GLN92, HIS64, TRP5, and HIS4 [58,59].The 6NM0 protein, on the other hand, showed two hydrogen bonds with TYR114 (H···OH) and LYS149 (O···HZ2) at bond distances of 2.0 Å and 2.2 Å, respectively. Hydrophobic interactions with the residues of PRO579, PRO580, THR584, LEU581, HIS588, MET525, GLY575, LYS576, and GLY577 further stabilized the active pocket. Stronger ligand-receptor interaction was indicated by this complex lower inhibition constant (2.18 μM) and effective binding energy (−7.72 kcal mol^{-1}) indicating enhanced binding affinity and higher inhibitory potency. The ligand efficiency (–0.28) and intermolecular energy (–8.92 kcal/mol) values reflect Stronger non-covalent interactions and stabilization of the ligand–protein complex, further supported by an improved hydrogen-bonding, van der Waals forces and desolvation energy (–8.66 kcal/mol). The electrostatic component (–0.26 kcal/mol) contributed to good interaction stability [60,61]. The 6NM0–ZPSD complex ultimately showed higher binding affinity and inhibitory potential than 3T6G–ZPSD, indicating that ZPSD interact with the 6NM0 target in an efficient manner and be a promising lead compound for anti-liver cancer activity.

3.12. Mathematical aspects of compound

The different degree-based topological indices that have been computed to aid in the comprehension of molecular physical characteristics and chemical reactivity are highlighted in this section. Drug molecules are represented as molecular graphs in theoretical chemistry, with atoms standing in for vertices and bonds for edges show in the Fig. 13. Edge partition data was used to derive topological descriptors for the compound under study. A set of vertices (V(G)) that represent atoms and a set of edges (E(G)) that represent bonds make up the molecular graph [62]. The total number of edges and vertices in the molecular graph determines its size and order, respectively. The number of bonds attached to a specific atom is indicated by the degree of each vertex, which is represented as d(u) and d(v). The molecular structure is analysed in this work using a variety of degree-based topological indices, as shown in Fig. 13 [63].

Definition 1. Trinajestic and Gutman created the first and second Zagreb indices, M1 (G) and M2(G) [64–66]

$$M1(G) = \sum_{uv \in E(G)} (du + dv)$$

and

$$M2(G) = \sum_{UV \in E(G)} (du.dv)$$

Definition 2. Harmonic index H(G) is [64–66] commuted as

$$H(G) = \sum_{UV \in E(G)} \frac{2}{du + dv}$$

Definition 3. explains the hyper Zagreb index [64–66] in the following way

$$HM(G) = \sum_{uv \in E(G)} (du + dv)^2$$

Table 10
Lipinski's values of ZPSD.

Descriptor	Value
Molecular Weight	412.94 g/mol
LogP	3.50
Acceptors	3
Donors	1
Surface Area	76.71° A

Table 9
NLO Properties of ZPSD.

Hyper Polarizabilities Calculations					
βxxx	−342.179	αxx	−216.022	μ x	0.6803
βxxy	−42.093	αxy	−23.9144	μ y	2.492
βxyy	−0.326	αyy	−172.996	μ z	−0.6803
βyyy	10.397	αxz	12.7249	μ (D)	2.6712
βzxx	64.074	αyz	−2.5766	μ (D)	8.91×10^{-30}Cm^{-1}
βxyz	−32.545	αzz	9.6701		
βzyy	−13.814	α (a.u)	−126.449		
βxzz	47.324	α (e.s.u)	$-1.8740E^{-23}$		
βyzz	0.4343	Δα (a.u)	427.8716		
βzzz	7.87	Δα (e.s.u)	$6.3411E^{-23}$		
βtot (a.u)	302.470	Δα C·m^2·V^{-1}	7.06×10^{-63}		
βtot (e.s.u)	$2.6131E^{-30}$				
βtot C^3·m^3·J^{-2}	9.3×10^{-40}				

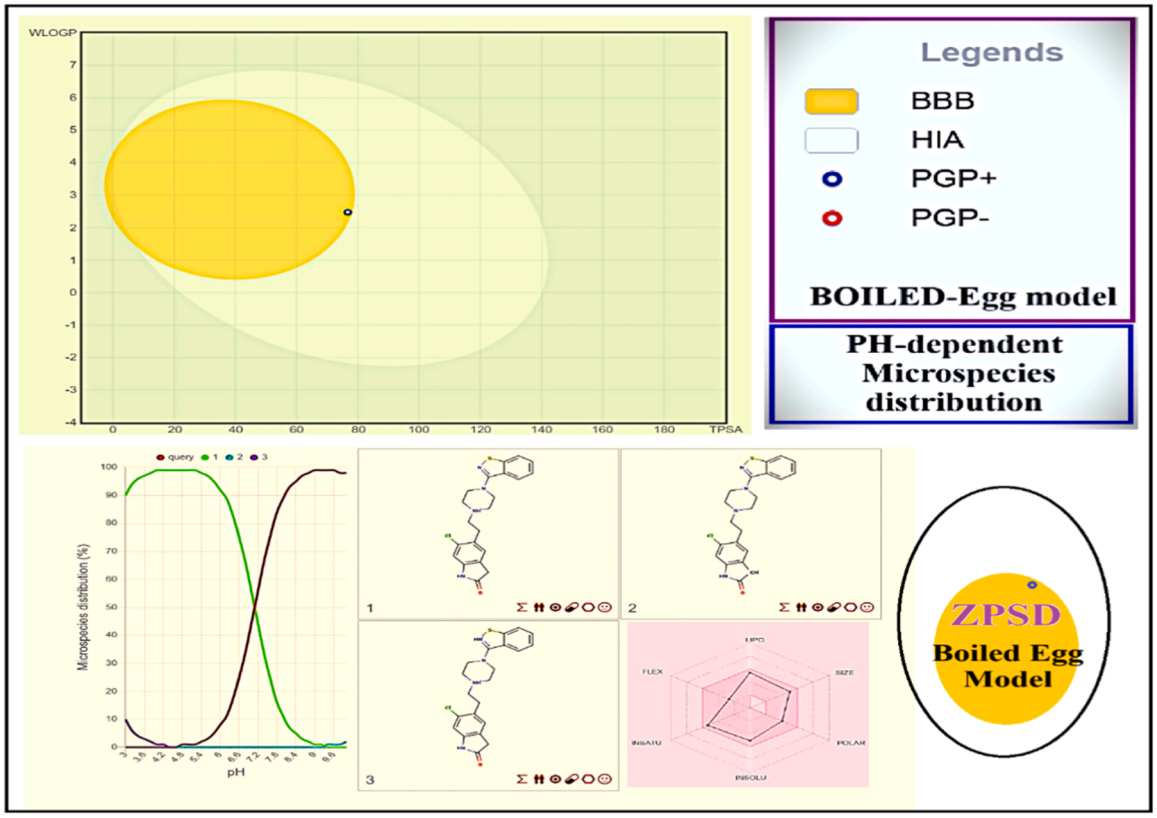

Fig. 11. BOILED-Egg Model of ZPSD.

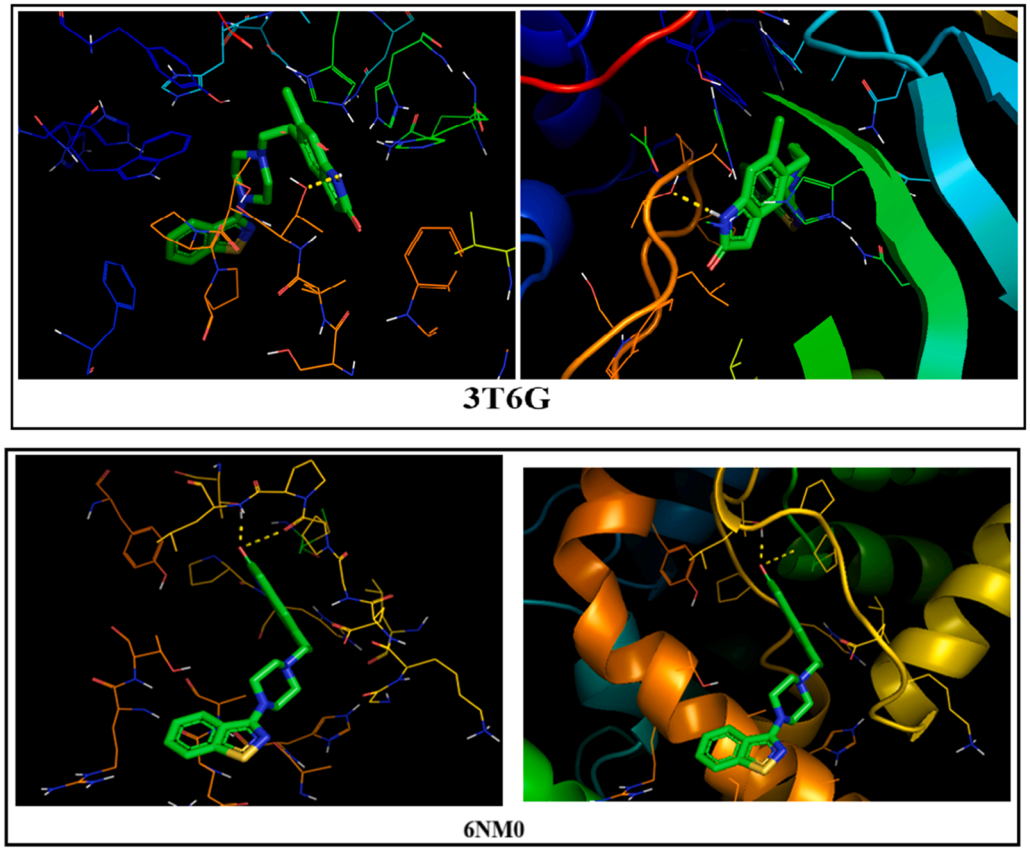

Fig. 12.a. Molecular Docking of ZPSD.

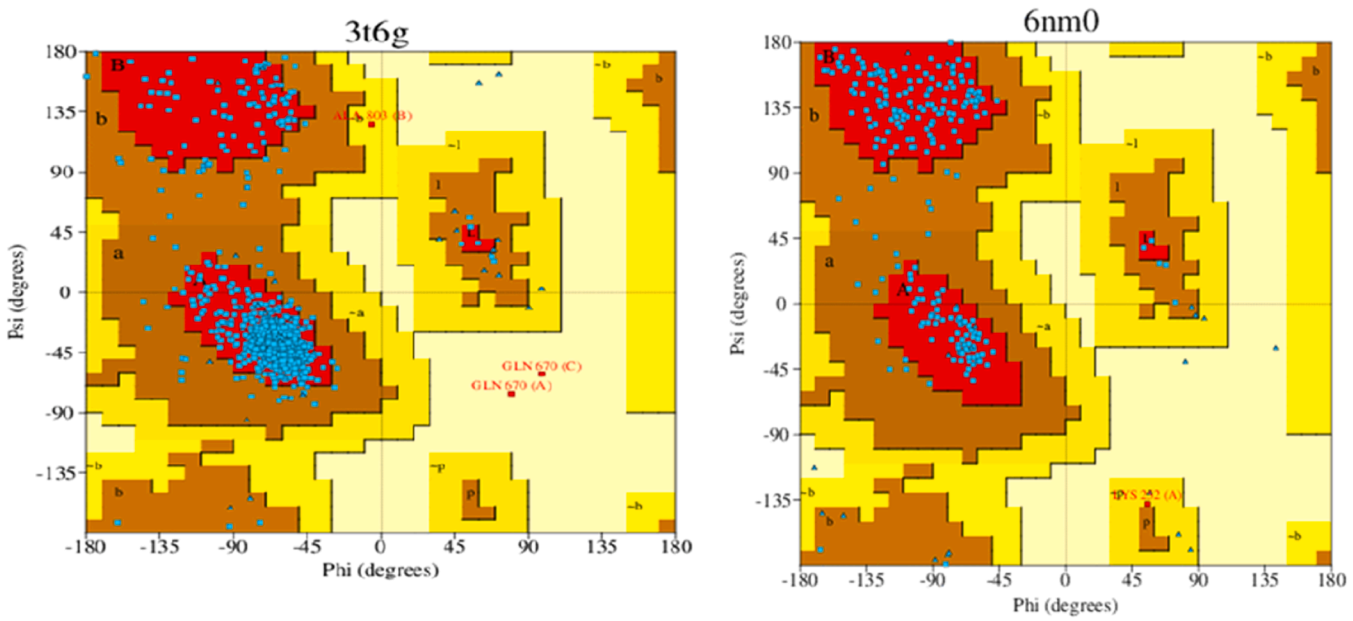

Fig. 12b. Ramachandran plot of protein.

Table 11
Binding energy of ZPSD.

Protein	Bonded residues	No. of. H bond	Bond distance (Å)	Estimated Inhibition Constant (μm)	Binding energy (kcal/mol)	RMSD (Å)	Amino acids	Hydrophobic interaction
3T6G	SER 582 (O… NH)	1	2.0	16.91	−6.75	91.44	THR- 199 LEU- 198	LEU-198 PRO-202 THR-200 ALA-65 ASN-67 GLN-92 HIS-64 TRP-5 HIS-4
6NM0	TYR 114 (H… OH) LYS 149 (O… HZ2)	2	2.0 2.2	2.18	−7.72	13.88	PRO - 580 PRO - 579 THR - 584	LEU-581 THR-584 PRO-579 HIS-588 MET-525 HIS-588 GLY-575 LYS-576 GLY-577

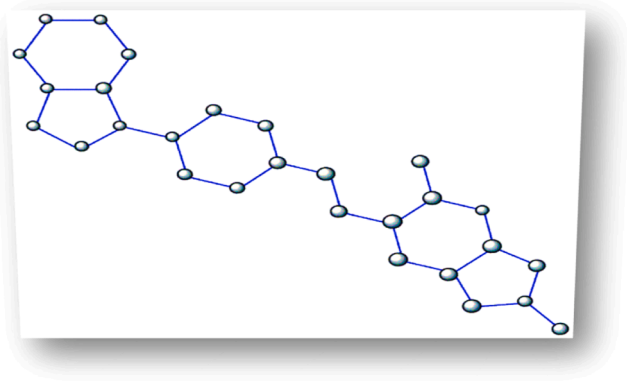

Fig. 13. QSPR Analytical Value of ZPSD.

Definition 4. The Forgotten index F(G) [60–62] is described as

$$F(G) = \sum_{uv \in E(G)} \left[(du)^2 \right| + \left| (dv)^2 \right]$$

Definition 5. The following one provides the Reciprocal Randic Index RR(G) [64–66] in its entirety.

$$RR(G) = \sum_{uv \in E(G)} \sqrt{du \times dv}$$

Definition 6. As cited in [64–66], the Randic index RA(G) is shown below.

$$RA(G) = \sum_{uv \in E(G)} \sqrt{\frac{1}{du \times dv}}$$

Definition 7. The Sum Connectivity S(G) [64–66], which is shown by

$$S(G) = \sum_{uv \in E(G)} \sqrt{\frac{1}{du + dv}}$$

Definition 8. geometric-arithmetic (GA) index [64–66] is interpreted as

$$GA(G) = \sum_{uv \in E(G)} \frac{2\sqrt{du \times dv}}{du + dv}$$

Definition 9. Atom Bond Connectivity Index ABC (G) [64–66] is given below

$$ABC(G) = \sum_{uv \in E(G)} \sqrt{\frac{du + dv - 2}{du \times dv}}$$

These degree-based topological indices were found using the edge partition approaches that we acquired using the hydrogen depletion of ZPSD (Fig. 13).

Theorem. *If G is the molecular graph of ZPSD molecules, then the many degree-based topological indices of G are mentioned below [64–66].*

$M1(ZPSD) = 122, M2(ZPSD) = 139, H(ZPSD) = 10.1, HM(ZPSD) = 895,$
$F(ZPSD) = 211, RR(ZPSD) = 139, RA(ZPSD) = 0.89, S(ZPSD) = 1.8,$
$GA(ZPSD) = 4.6, ABC(ZPSD) = 2.85.$

Proof. Assume that G is the ZPSD graph and that E(i,j) is the class of edges that link vertices of degree i to degree j. From the Fig. 13 observe that $|E_{1,3}| = 2$, $|E_{2,2}| = 7$, $|E_{2,3}| = 5$, $|E_{3,2}| = 5$, $|E_{3,3}| = 5$. (Table 12)

i) The following is the outcome of applying Definition 1:

$$M1(ZPSD) = 2(1+3) + 7(2+2) + 5(2+3) + 5(3+2) + 5(3+3) = 122$$

and

$$M2(ZPSD) = 2(1\times 3) + 7(2\times 2) + 5(2\times 3) + 5(3\times 2) + 5(3\times 3) = 139$$

ii) The following is the outcome of applying Definition 2:

$$H(ZPSD) = 2 \times \frac{2}{1+3} + 5 \times \frac{2}{2+2} + 5 \times \frac{2}{2+3} + 5 \times \frac{2}{3+2} + 5 \times \frac{2}{3+3} = 10.1$$

iii) The following is the outcome of applying Definition 3:

$$HM(ZPSD) = 2x(1+3)^2 + 7(2+2)^2 + 5(2+3)^2 + 5(3+2)^2 + 5(3+3)^2 = 895$$

iv) The result of using Definition 4 is as follows:

$$F(ZPSD) = 2\left[1^2+3^2\right] + 5\left[2^2+2^2\right] + 15\left[2^2+3^2\right] + 2\left[3^2+2^2\right] + 2\left[3^2+3^2\right] = 211$$

v) The result of using Definition 5 is as follows:

$$RR(ZPSD) = 2\sqrt{1\times 3} + 7\sqrt{2\times 2} + 5\sqrt{2\times 3} + 2\sqrt{3\times 2} + 2\sqrt{3\times 3} = 139$$

vi) The result of using Definition 6 is as follows:

$$RA(ZPSD) = 2 \times \sqrt{\frac{1}{1\times 3}} + 7 \times \sqrt{\frac{1}{2\times 2}} + 5\sqrt{\frac{1}{2\times 3}} + 5\sqrt{\frac{1}{3\times 2}} + 5 \times \sqrt{\frac{1}{3\times 3}} = 0.89$$

vii) The following is the outcome of applying Definition 7:

$$S(ZPSD) = 2 \times \sqrt{\frac{1}{10}} + 7 \times \sqrt{\frac{1}{8}} + \left(5 \times \sqrt{\frac{1}{13}}\right)^2 + 5 \times \sqrt{\frac{1}{18}} = 1.8$$

viii) The following is the outcome of applying Definition 8:

$$GA(ZPSD) = 2\left(\frac{2\sqrt{1\times 3}}{1+3}\right) + 7\left(\frac{2\sqrt{2\times 2}}{2+2}\right) + 5\left(\frac{2\sqrt{2\times 3}}{2+3}\right) + 5\left(\frac{2\sqrt{3\times 2}}{3+2}\right) + 5\left(\frac{2\sqrt{3\times 3}}{3+3}\right) = 4.6$$

ix) The following is the outcome of applying Definition 9:

$$ABC(ZPSD) = 2\sqrt{\frac{1+3-2}{1\times 3}} + 7\sqrt{\frac{2+2-2}{2\times 2}} + 5\sqrt{\frac{2+3-2}{2\times 3}} + 5\sqrt{\frac{3+2-2}{3\times 2}} + 5\sqrt{\frac{3+3-2}{3\times 3}} = 2.85$$

The Table 10 shows, the structural descriptors were investigated an electronic responsiveness and binding potential, as

Table 12
Physical and Math Comparative Of ZPSD.

S. No	Physical and Chemical Properties	Physical and Chemical Properties Values	Mathematical QSPR Analytical Value.
1	β tot, μ (D)	2.6131E^{-30}; 2.67126939	ABC(ZPSD) = 3
2	Melting Point	206–215 °C	F(ZPSD) = 211
3	C8 NMR shift	124	M1 (ZPSD) =122
4	Δα (e.s.u)	6.3411E^{-23}	H (ZPSD)=10.1
5	E_{Lumo}	1.0	RA(ZPSD) = 1
7	Δr index, Binding energy (kcal/mol)	4.579; 6.0,7.0	GA(ZPSD) = 5
6	LogP; Bond distance (Å) from docking; Estimated Inhibition Constant (μm)	3.50, 2.0;2.2, 2.18	S(ZPSD) = 2

shown by the QSPR correlation analysis, which shows that higher ABC, H, and GA values are directly proportional to both β_tot and docking affinity (R2 = 0.87). By connecting ZPSD's physicochemical properties to its bioactivity and optoelectronic behaviour, this robust statistical relationship creates a logical structure property activity correlation (SPAC). Bond distance (Å) from docking, Estimated Inhibition Constant (μm) of ZPSD exhibited anticancer properties, which is a promising molecule with both bioactive and nonlinear optical potential because the mathematical QSPR indices (ABC, F, M_1, H, RA, S, GA) together offer a consistent and quantitative framework that links electronic structure, spectroscopic observables and biological interaction tendencies [64–66].

4. Conclusion

As a result of its unique electronic structure, conjugated π-systems, and heteroatoms that improve charge-transfer and hydrogen bonding of ZPSD exhibits great promise for therapeutic repurposing against liver cancer. While B3LYP/6–311++*G*(d,p) basis set of DFT and TD-DFT studies validated optimized geometry range of Bond length as 1.38 to 1.54 Å, Typical aromatic or flexible Bond angle are matched by chain and ring angles that fall between 118° and 130°, such as C_{25}–C_{26}–C_{27} and C_{24}–C_{28}–C_{27}, stability, and close agreement between theoretical and experimental energy gaps, spectroscopic analyses (FT-IR, UV–Vis, NMR) confirmed its structural integrity and its key functional groups such as amide, aromatic, and heteroaromatic moieties, which contribute to π–π stacking and hydrogen bonding interactions for bioactivity. Both electrophilic (C, S, Cl) and nucleophilic (O, N) reactive sites were found using Mulliken, MEP analyses, and intramolecular charge delocalization that contributes to molecular stability was validated through the lone pair from Cl_{11} and π*(C_6–C_7) (13.0 kcal/mol) and π*(C_{23}–C_{24}) (23.4 kcal/mol) by NBO results. Receptor adaptability was supported by strong electron delocalization and van der Waals interactions found in topological analyses (ELF, LOL, and RDG). strong Charge transfer of State III exhibited the Large electron-hole separation enhances the ability to interfere with the high ROS potential which is selectively potent in biomolecular targets. photodynamic killing of cancer cells. SwissADME results indicated that ZPSD obeys Lipinski's rule of five, ensuring drug-likeness, while the boiled egg model reveals the chlorine substituent enhances lipophilicity and cellular permeability. and high anisotropic polarizability (Δα = 427.87 a.u., 6.3411 × 10^{-23} esu, $7.06\times10^{-63C}\cdot m^2\cdot V^{-1}$) and favourable QSPR indices (ABC, F, M_1, H, RA, S, GA) correlations show efficient bioactive behaviour. The ZPSD–6NM0 complex demonstrated a greater binding affinity (–7.72 kcal/mol) through TYR114 and LYS149 interactions, according to molecular docking, indicating stable and specific binding within the liver cancer receptor site. Together, these findings highlight ZPSD's potent electronic, structural, and pharmacokinetic properties as a prospective lead molecule for liver anticancer drug.

CRediT authorship contribution statement

S. Kayashrini: Writing – original draft, Formal analysis, Data curation. **P. Rajesh:** Writing – original draft, Supervision, Software. **M. Kesavan:** Methodology. **A. Kala:** Writing – review & editing, Validation. **M. Pavithra:** Data curation.

Declaration of competing interest

The authors declare that they have no known competing financial interests or personal relationships that could have appeared to influence the work reported in this paper.

Supplementary materials

Supplementary material associated with this article can be found, in the online version, at doi:10.1016/j.molstruc.2025.144847.

Data availability

Data will be made available on request.

References

[1] A. Martínez, I.A. Ibarra, R. Vargas, A quantum chemical approach representing a new perspective concerning agonist and antagonist drugs in the context of schizophrenia and Parkinson's disease, PLoS. One 14 (12) (2019) e0224691, https://doi.org/10.1371/journal.pone.0224691.

[2] M.A. Mancano, Ziprosidone-induced transient agranulocytosis; delayed onset of cardiac adverse effects with fingolimod; telmisartan-induced myotoxicity; severe dilated cardiomyopathy induced by adalimumab and ustekinumab, Hosp. Pharm. 50 (10) (2015) 855–858, https://doi.org/10.1310/hpj5010-855.

[3] P. Wright, A. Alex, F. Pullen, Predicting collision-induced dissociation spectra: semi empirical calculations as a rapid and effective tool in software-aided mass spectral interpretation, Rapid Commun. Mass Spectrom. 28 (10) (2014) 1127–1143, https://doi.org/10.1002/rcm.6870.

[4] P.U. Preetha, M. Suresh, Structure property modeling of physicochemical properties of antipsychotic drugs via topological descriptors, multigraph modeling with the specific treatment of heteroatoms and chemometric methods, IAENG Int. J. Appl. Math. 54 (11) (2024) 2388–2403. Retrieved from, https://www.proquest.com/scholarly-journals/structure-property-modeling-physicochemical/docview/3156613531/se-2.

[5] S. Ünal, M. Karakaplan, E. Öz, İ. Yılmaz, S. Altın, A. Bayri, Why is Clozapine more effective than other Atypical antipsychotics? Density functional theory and molecular docking approach, Bartın Univ. Int. J. Nat. Appl. Sci. 2 (2) (2019) 207–215, https://doi.org/10.34108/eujhs.885229.

[6] G. Ribaudo, M. Bortoli, C. Pavan, G. Zagotto, L. Orian, Antioxidant potential of psychotropic drugs: from clinical evidence to in vitro and in vivo assessment and toward a new challenge for in silico molecular design, Antioxidants 9 (8) (2020) 714, https://doi.org/10.3390/antiox9080714.

[7] A. Badran, A. Tul-Wahab, H. Zafar, N. Mohammad, R. Imad, M. Ashfaq Khan, E. Baydoun, M.I. Choudhary, Antipsychotics drug aripiprazole as a lead against breast cancer cell line (MCF-7) in vitro, PLoS. One 15 (8) (2020) e0235676, https://doi.org/10.1371/journal.pone.0235676.

[8] J.R. Jacob, K. Palanichamy, A. Chakravarti, Antipsychotics possess anti-glioblastoma activity by disrupting lysosomal function and inhibiting oncogenic signaling by stabilizing PTEN, CDD 15 (2024) 414, https://doi.org/10.1038/s41419-024-06779-3.

[9] A. Sahu, S. Ahmad, K. Imtiyaz, A. Kizhakkeppurath Kumaran, M. Islam, K. Raza, M. Easwaran, A.K. Kunnath, M.A. Rizvi, S. Verma, In-silico and in-vitro study reveals ziprasidone as a potential aromatase inhibitor against breast carcinoma, Sci. Rep. 13 (2023) 16545, https://doi.org/10.1038/s41598-023-43789-1.

[10] N. Vlachos, M. Lampros, S. Voulgaris, G.A. Alexiou, Repurposing antipsychotics for cancer treatment, Biomedicines. 9 (12) (2021) 1785, https://doi.org/10.3390/biomedicines9121785.

[11] S. Lee, W. Park, C.H. Choi, Expanding horizons in quantum chemical studies: the versatile power of mrsf-tddft, Acc. Chem. Res 58 (2) (2020) 208–217, https://doi.org/10.1021/acs.accounts.4c00640.

[12] S. Kayashrini, P. Rajesh, E. Dhanalakshmi, M. Kesavan, M. Prabhaharan, D.A. Al Farraj, M.S. Elshikh, FT-IR, UV–Vis, density functional theory and molecular docking studies on 3, 7, 11, 15-tetramethyl-2hexadecen-1-ol, J. Mol. Struct. 1321 (2025) 139600, https://doi.org/10.1016/j.molstruc.2024.139600.

[13] J.J. Laura, P. Rajesh, M. Kesavan, E. Dhanalakshmi, S. Kayashrini, M. Prabhaharan, Degree–based topological indices, NMR chemical shifts, chemical reactivity, molecular dynamics and DFT analysis of 1, 4-methanoazulene-9-methanol, decahydro-4, 8, 8-trimethyl-,[1S-(1α, 3aβ, 4α, 8aβ, 9R)], Biophys. Chem. 322 (2025) 107442, https://doi.org/10.1016/j.bpc.2025.107442.

[14] C. Zheng, S. Li, W. Fang, Y. Zhang, F. Liu, W. Zhang, Z. Men, Exploring the solvent regulated electron status properties of astaxanthin by Raman spectroscopy and DFT simulation, Spectrochim. Acta A: Mol. Biomol. Spectrosc. (2025) 126635, https://doi.org/10.1016/j.saa.2025.126635.

[15] P. Rajesh, S. Gunasekaran, T. Gnanasambandan, S. Seshadri, Experimental, quantum chemical and NBO/NLMO investigations of pantoprazole, Spectrochim. Acta A: Mol. Biomol. Spectrosc. 136 (2015) 247–255, https://doi.org/10.1016/j.saa.2014.09.029.

[16] P. Rajesh, S. Gunasekaran, S. Seshadri, T. Gnanasambandan, DFT computational analysis of piracetam, Spectrochim. Acta A: Mol. Biomol. Spectrosc. 132 (2014) 249–255, https://doi.org/10.1016/j.saa.2014.04.106.

[17] L.D. Mendelsohn, ChemDraw 8 ultra, windows and macintosh versions, J. Chem. Inf. Comput. Sci. 44 (2004) 2225–2226, https://doi.org/10.1021/ci040123t.

[18] P. Rajesh, S. Gunasekaran, T. Gnanasambandan, S. Seshadri, Molecular structure and vibrational analysis of trifluoperazine by FT-IR, FT-raman and UV–Vis spectroscopies combined with DFT calculations, Spectrochim. Acta A: Mol. Biomol. Spectrosc. 137 (2015) 1184–1193, https://doi.org/10.1016/j.saa.2014.08.100.

[19] K. Nikolic, M. Pavlovic, A. Smolinski, D. Agbaba, The chemometric study and quantitative structure retention relationship modeling of liquid chromatography

separation of ziprasidone components, Comb. Chem. High Throughput Screen 15 (9) (2012) 730–744, https://doi.org/10.2174/138620712803519699.
[20] A. Sipos, S. Berényi, Formation of novel 1, 3-thiazole-and 1, 2-thiazole-fused aporphines and study on the simultaneously occurring benzothiazole–benzisothiazole-type isomerization, Monatsh. Chem.-Chem. Mon. 140 (4) (2009) 387–396, https://doi.org/10.1007/s00706-008-0038-x.
[21] K. Kula, A. Łapczuk-Krygier, A DFT computational study on the [3+ 2] cycloaddition between parent thionitrone and nitroethene, Curr. Chem. Lett 7 (2018) 27–34, https://doi.org/10.5267/j.ccl.2018.02.001.
[22] A. Kyrychenko, I. Bylov, A. Geleverya, S. Kovalenko, I. Zhuravel, V. Fetyukhin, T. Langer, Computer-aided rational design and synthesis of new potential antihypertensive agents among 1, 2, 3-triazole-containing nifedipine analogs, Sci.: Pharm. Sci. 3 (2024) 4–12, https://doi.org/10.15587/2519-4852.2024.291626.
[23] S.B. Marganakop, R.R. Kamble, M.S. Sannaikar, P.K. Bayannavar, S.M. Kumar, S. R. Inamdar, A.M. Shirahatti, S.M. Desai, S.D.S Joshi, DFT and molecular docking based structural analyses towards novel 3-piperazin-1-yl-benzo [d] isothiazole and 3-piperidin-4-yl-benzo [d] isoxazoles appended to quinoline as pharmacological agents, J. Mol. Struct. 1248 (2022) 131442, https://doi.org/10.1016/j.molstruc.2021.131442.
[24] H. Tanikawa, K. Ishii, S. Kubota, T. Sasanuma, S. Yagai, A. Kitamura, T. Karatsu, Effect of nitro-substitution on the photochemistry of 3-piperidino-1, 2-benzisothiazole derivatives: a mechanistic investigation, Heterocycles. 81 (3) (2010) 659, https://doi.org/10.3987/COM-09-11889 (2010).
[25] A.G. Nozad, H. Najafi, S. Meftah, M. Aghazadeh, A systematic study on hydrogen bond interactions in sulfabenzamide: DFT calculations of the N-14, O-17, and H-2 NQR parameters, Biophys. Chem 139 (2–3) (2009) 116–122, https://doi.org/10.1016/j.bpc.2008.10.010.
[26] A.G. Nozad, S. Meftah, M.H. Ghasemi, R.A. Kiyani, M. Aghazadeh, Investigation of intermolecular hydrogen bond interactions in crystalline L-cysteine by DFT calculations of the oxygen-17, nitrogen-14, and hydrogen-2 EFG tensors and AIM analysis, Biophys. Chem 141 (2009) 49–58.
[27] J.A. Kaduk, K. Zhong, A.M. Gindhart, T.N. Blanton, Crystal structure of ziprasidone hydrochloride monohydrate, C21H22Cl2N4OS (H2O), Powder. Diffr. 30 (2015) 192–198, https://doi.org/10.1017/S0885715615000305.
[28] D. Obradović, F. Andrić, M. Zlatović, D. Agbaba, Modeling of Hansen's solubility parameters of aripiprazole, ziprasidone, and their impurities: a nonparametric comparison of models for prediction of drug absorption sites, J. Chemom. 32 (4) (2018) e2996, https://doi.org/10.1002/cem.2996.
[29] K. Poluri, E.S.T.H.E.R. Mulpur, S.B. Puttugunta, K.B. Govada, Formulation development and evaluation of novel oral soluble films of ziprasidone hydrochloride in the treatment of schizophrenia, Int J Pharm Pharm Sci 5 (2013) 619–627. ISSN- 0975-1491.
[30] R.S. Mulliken, Electronic population analysis on LCAO–MO molecular wave functions, J. Chem. Phys 23 (10) (1955) 1833–1840, https://doi.org/10.1063/1.1740588.
[31] R. Carbó-Dorca, P. Bultinck, Quantum mechanical basis for Mulliken population analysis, J. Math. Chem 36 (3) (2004) 231–239, https://doi.org/10.1023/B:JOMC.0000044221.23647.20.
[32] P. Rajesh, S. Gunasekaran, T. Gnanasambandan, S. Seshadri, Experimental and theoretical study of ornidazole, Spectrochim. Acta A: Mol. Biomol. Spectrosc. 153 (2016) 496–504, https://doi.org/10.1016/j.saa.2015.08.032 (2013).
[33] A.K. Mishra, S.P. Tewari, Density functional theory calculations of spectral, NLO, reactivity, NBO properties and docking study of vincosamide-N-oxide active against lung cancer cell lines H1299, SN Appl. Sci. 2 (2020) 1021, https://doi.org/10.1007/s42452-020-2842-9.
[34] E. Dhanalakshmi, P. Rajesh, M. Anbarasu, P. Kandan, A. Raaza, M. Prabhaharan, D. F.T. GCMS–, E.L.F. LOL, NCI-RDG, kinetic energy, reactivity, stability, topological molecular descriptors evaluation on 2-propanone, 1-hydroxy-, isopropyl alcohol and glycerin: for NLO application, Indian J. Biochem. Biophys. (IJBB) 62 (2025) 615–631, https://doi.org/10.56042/ijbb.v62i6.10790.
[35] A. Suvitha, S. Periandy, S. Boomadevi, M. Govindarajan, Vibrational frequency analysis, FT-IR, FT-raman, ab initio, HF and DFT studies, NBO, HOMO–LUMO and electronic structure calculations on pycolinaldehyde oxime, Spectrochim. Acta A 117 (2014) 216–224, https://doi.org/10.1016/j.saa.2013.07.080.
[36] P. Politzer, D.G. Truhlar, Chemical Applications of Atomic and Molecular Electrostatic Potentials, Plenum Press, 1981. https://link.springer.com/book/10.1007/978-1-4757-9634-6.
[37] V. Fung, G. Hu, P. Ganesh, B.G. Sumpter, Machine learned features from density of states for accurate adsorption energy prediction, Nat. Commun. 12 (2021) 88, https://doi.org/10.1038/s41467-020-20342-6.
[38] B.S.M. Rahman, Study of Structure, Band, and Density of States Properties of $TlPbCl_3$ with DFT Based on First-Principles Calculations (Doctoral dissertation, Department of Physics, Bangabandhu Sheikh Mujibur Rahman Science and Technology University). https://www.researchgate.net/publication/386262915, 2024.
[39] A.N.J.U. Gauniya, R.U.P.A. Mazumder, K.A.M.L.A. Pathak, Formulation, optimization and characterization of ziprasidone nanocrystals prepared by media milling technique, Int. J. Pharm. Pharm. Sci 7 (2015) 146–150. https://www.researchgate.net/publication/282642319.
[40] K.S. Jadhav, B.E. Kiran, Solubility enhancement and formulation of fast dissolving tablets of ziprasidone hydrochloride, Int. J. Res. Pharm. Chem. 6 (2016) 675–683. ISSN: 2231-2781, www.ijrpc.com.
[41] A. Shafi, R.D. Timiri Sathyamurthy, J. Seetharaman, M. Sambanthan, R. Murugesan, S. Sundaram, R.B. Ramarathinam, Molecular docking, quantum chemical computational and vibrational studies on bicyclic heterocycle "6-nitro-2,3-dihydro-1,4-benzodioxine": anti-cancer agent, Comput. Biol. Chem. j. Compbiolchem 86 (2020), https://doi.org/10.1016/j.compbiolchem.2020.107226, 2020.107226.
[42] P. Divya, P. Muthuraja, M. Dhandapani, V.B. Jothy, Hydrogen bonding interactions on molecular properties of pesticidal compound 4-nitrophthalic acid: experimental density functional theory computations, electron localized function, localized orbital locator analysis and molecular docking scrutiny, Spectrosc. Lett (2022), https://doi.org/10.1080/00387010.2022.2080227.
[43] EA. Adindu, O.C. Godfrey, E.I.ABO.EDC. Agurokpon, S.E. Ogbodo, I. Benjamin, H. Louis, Structural analysis, reactivity descriptors (HOMO-LUMO, ELF, NBO), effect of polar (DMSO, EtOH, H2O) solvation, and libido-enhancing potential of resveratrol by molecular docking, Chem. Phys. Impact 7 (2023), https://doi.org/10.1016/j.chphi.2023.100296.
[44] AS. Kazachenko, E. Tanış, F. Akman, M. Medimagh, N. Issaoui, O. Al-Dossary, LG. Bousiakou, AS. Kazachenko, D. Zimonin, AM. Skripnikov, A comprehensive study of N-butyl-1H-benzimidazole, Molecules. 27 (2022), https://doi.org/10.3390/molecules27227864.
[45] S. Sevvanthi, S. Muthua, S. Aayisha, P. Rameshe, M. Raja, Spectroscopic (FT-IR, FT-Raman and UV–Vis), computational (ELF, LOL, NBO, HOMO-LUMO, Fukui, MEP) studies and molecular docking on benzodiazepine derivativesheterocyclic organic arenes, Chem. Data Collect 30 (2020), https://doi.org/10.1016/j.cdc.2020.100574.
[46] P. Manjusha, J.C. Prasana, S. Muthu, B. Fathima Rizwana, Spectroscopic elucidation (FT-IR, FT-Raman and UV-visible) with NBO, NLO, ELF, LOL, drug likeness and molecular docking analysis on 1-(2-ethylsulfonylethyl)- 2-methyl-5-nitro-imidazole: an antiprotozoal agent, Comput. Biol. Chem. 88 (2020), https://doi.org/10.1016/j.compbiolchem.2020.107330.
[47] D.C. Holland, A.R. Carroll, Structure revision of formyl phloroglucinol meroterpenoids: a unified approach using NMR fingerprinting and DFT NMR and ECD analyses, Molecules. 29 (3) (2024), https://doi.org/10.3390/molecules29030594.
[48] P.MA Mekoung, A. Malloum, M. Govindarajan, R.N. Mballa, I. Patouossa, A. Abouem A Zintchem, C.P.N. Nanseu, I.N. Mbouombouo, Spectroscopic properties (FT-IR, NMR and UV) and DFT studies of amodiaquine, Heliyon. 9 (12) (2023), https://doi.org/10.1016/j.heliyon.2023.e22187.
[49] F. Nardelli, S. Borsacchi, L. Calucci, E. Carignani, F. Martini, M. Geppi, Anisotropy and NMR spectroscopy. Rendiconti Lincei, Springer, 2020, pp. 999–1010, https://doi.org/10.1007/s12210-020-00945-3, 31.
[50] H. Huang, N. Li, S. Fu, X. Mo, X. Cao, X. Yin, C. Yang, Pure polycyclic aromatic hydrocarbon isomerides with delayed fluorescence and anti-kasha emission: high-efficiency non-doped fluorescence OLEDs, Adv. Sci. 10 (31) (2023) 2304204, https://doi.org/10.1002/advs.202304204.
[51] P.R MohamedHisam, E. Dhanalakshmi, J.J.A. Laura, M. Prabhaharan, G. Jayaraman, Topological characterization, computational, spectroscopic (FT-IR, 1H, 13C NMR) exploration, chemical reactivity analysis of 6-(3,3-dimethyl-oxiran-2-ylidene)-5,5-dimethyl-hex-3-en-2-one, Next Mater. 8 (2025) 100831, https://doi.org/10.1016/j.nxmate.2025.100831.
[52] G. Sudhakar, D.R Babu, Synthesis and characterization of piperazine nitrate monochloride semi-organic single crystal for NLO applications, Discov. Appl. Sci. 6 (12) (2024) 645, https://doi.org/10.1007/s42452-024-06341-y.
[53] K.J. Hamam, M.I. Alomari, A study of the optical band gap of zinc phthalocyanine nanoparticles using UV–Vi's spectroscopy and DFT function, Appl. Nanosci. 7 (2017) 261–268, https://doi.org/10.1007/s13204-017-0568-9.
[54] N. Elangovan, S. Sowrirajan, N. Arumugam, B. Rajeswari, S. Mathew, C.G. Priya, B. R. Venkatraman, S.M. Mahalingam, Theoretical investigation on solvents effect in molecular structure (TD-DFT, MEP, HOMO-LUMO), topological analysis and molecular docking studies of n-(5-((4-ethylpiperazin-1-yl) methyl) pyridin-2-yl)-5-fluoro-4-(4-fluoro-1-isopropyl-2-methyl-1H-benzo [d] imidazol-6-yl) pyrimidin-2-amine, Polycycl. Aromat. Compd. 44 (2024) 4467–4490, https://doi.org/10.1080/10406638.2023.2254896.
[55] M. Perveen, S. Nazir, A.W. Arshad, M.I. Khan, M. Shamim, K. Ayub, M.A. Khan, J. Iqbal, Therapeutic potential of graphitic carbon nitride as a drug delivery system for cisplatin (anticancer drug): a DFT approach, Biophys. Chem 267 (2020) 106461, https://doi.org/10.1016/j.bpc.2020.106461.
[56] V. Kinare, A.S. Shetty, A. Suresh, S. Tole, PAX6 can substitute for LHX2 and override NFIA-induced astrogliogenesis in developing hippocampus in vivo, J. Biosci 43 (1) (2018) 75–83, https://doi.org/10.1007/s12038-018-9731-z (2018).
[57] J.H. Nie, T. Yang, H. Li, H.S. Ye, G.Q. Zhong, T.T. Li, C. Zhang, W.H. Huang, J. Xiao, Z. Li, J.L. He, Identification of GPC3 mutation and upregulation in a multidrug resistant osteosarcoma and its spheroids as therapeutic target, J. Bone Oncol. 30 (2025) 100391, https://doi.org/10.1016/j.jbo.2021.100391.
[58] E. Díaz-Cervantes, A. Islas-Jácome, A. Renteria-Gomez, J. Robles, R. Gámez-Montaño, In vitro and in silico evaluation of twelve newly-synthesized 1-acetamide-5-methoxy-2-oxindoles as 5-Ht7 receptor ligands, Bioorg. Med. Chem. Lett 25 (2015) 1580–1585, https://doi.org/10.1016/j.bmcl.2015.02.008 (2015).
[59] M. Jablonský, M. Štekláč, V. Majova, M. Gall, J. Matúška, M. Pitoňák, L. Bučinský, Molecular docking and machine learning affinity prediction of compounds identified upon softwood bark extraction to the main protease of the SARS-CoV-2 virus, Biophys. Chem 288 (2025) 106854, https://doi.org/10.1016/j.bpc.2022.106854.
[60] R. Ekhteiari Salmas, Y. Serhat Is, S. Durdagi, M. Stein, M. Yurtsever, A QM protein–ligand investigation of antipsychotic drugs with the dopamine D2 receptor (D2R), J. Biomol. Struct. Dyn. 36 (2018) 2668–2677, https://doi.org/10.1080/07391102.2017.1365772.
[61] E. Díaz-Cervantes, A. Islas-Jácome, A. Renteria-Gomez, J. Robles, R. Gámez-Montaño, In vitro and in silico evaluation of twelve newly-synthesized 1-

acetamide-5-methoxy-2-oxindoles as 5-Ht7 receptor ligands, Bioorg. Med. Chem. Lett 25 (2015) 1580–1585, https://doi.org/10.1016/j.bmcl.2015.02.008.
[62] B. Kirana, M.C. Shanmukha, A. Usha, A QSPR analysis and curvilinear regression models for various degree-based topological indices: quinolone antibiotics, Heliyon. 10 (12) (2024), https://doi.org/10.21203/rs.3.rs-3887676 /v1 (2024).
[63] I. Gutman, Degree based topological indices, Croat. Chem. Acta 86 (2013) 351–361, https://doi.org/10.5562/cca2294.
[64] B. Furtula, I. Gutman, A forgotton topological index, J. Math. Chem 53 (2015) 213–220, https://doi.org/10.1007/s10910-015-0480-z.
[65] I. Gutman, B. Furtula, C. Elphick, Three new/old Vertex-degree-based topological indices, Commun. Math. Comput. Chem 72 (2014). https://www.researchgate.net/publication/279602396.
[66] M.R. Farahani, On the Randic and Sum-connectivity index of nanotubes, Ann. West Univ. Timis.-Math. Comput. Sci. 51 (2013) 39–46, https://doi.org/10.2478/awutm-2013-0014.